Research Paper

GEOSPHERE

GEOSPHERE, v. 15

https://doi.org/10.1130/GES02070.1

13 figures; 4 tables

CORRESPONDENCE: palasino@conicet.gov.ar

CITATION: Alasino, P.H., Ardill, K., Stanback, J., Paterson, S.R., Galindo, C., and Leopold, M., 2019, Magmatically folded and faulted schlieren zones formed by magma avalanching in the Sonora Pass Intrusive Suite, Sierra Nevada, California: Geosphere, v. 15, https://doi.org/10.1130/GES02070.1.

Science Editor: Shanaka de Silva
Associate Editor: Alan Whittington

Received 28 September 2018
Revision received 30 April 2019
Accepted 3 July 2019

Magmatically folded and faulted schlieren zones formed by magma avalanching in the Sonora Pass Intrusive Suite, Sierra Nevada, California

P.H. Alasino[1,2,*], K. Ardill[3,*], J. Stanback[3,*], S.R. Paterson[3,*], C. Galindo[4,*], and M. Leopold[5,*]

[1]Centro Regional de Investigaciones Científicas y Transferencia Tecnológica de La Rioja (Prov. de La Rioja–UNLaR–SEGEMAR–UNCa–CONICET), Entre Ríos y Mendoza s/n, Anillaco 5301, Argentina
[2]Instituto de Geología y Recursos Naturales, Centro de Investigación e Innovación Tecnológica, Universidad Nacional de La Rioja (INGeReN-CENIIT-UNLaR), Av. Gob. Vernet y Apóstol Felipe, 5300 La Rioja, Argentina
[3]Department of Earth Sciences, University of Southern California, 3651 Trousdale Parkway, Los Angeles, California 90089-0740, USA
[4]Departamento de Mineralogía y Petrología, Universidad Complutense de Madrid–Instituto de Geociencias (UCM-CSIC), 28040 Madrid, Spain
[5]Department of Geology, School of Science, Math, and Engineering, San Juan College, 4601 College Boulevard, Farmington, New Mexico 87402, USA

ABSTRACT

The southwestern margin of the Late Cretaceous Sonora Pass Intrusive Suite, northern Sierra Nevada, California (USA), preserves a densely populated zone of magmatic structures that record dynamic magmatic layer formation and deformation (faulting and folding) within a solidifying upper-crustal magma mush. This zone consists largely of coupled melanocratic (or schlieren) and leucocratic bands hosted within the 95.6 ± 1.5 Ma Kinney Lakes granodiorite (Leopold, 2016), with orientations approximately parallel to the intrusive margin and with inward younging directions. Schlieren consist of a high modal abundance of medium-grained ferromagnesian minerals (hornblende + biotite), zircon, sphene, apatite, opaque minerals, and minor plagioclase and interstitial quartz. Leucocratic bands are dominated by coarse-grained feldspar + quartz with minor ferromagnesian and accessory minerals. Whole-rock geochemical and Sr and Nd isotopic data indicate that the schlieren are derived from the Kinney Lakes granodiorite by effective mechanical separation of mafic minerals and accessory phases.

We interpret that the schlieren zone at the margin of the Kinney Lakes granodiorite formed by large-scale collapse of crystal mush by "magma avalanching," facilitated by gravity, local convection, and possibly by host-rock stoping at the margin. This process eroded a significant portion of the solidifying margin of the chamber and resulted in the formation of magmatically deformed layered structures, which experienced further mingling, re-intrusion, magmatic erosion, and recycling processes. We envisage that magma avalanching of magma mushes in plutons can be achieved by any unstable process (e.g., tectonic, fluid-assisted, stoping, or gravity-driven) in large, long-lived magma-mush chambers.

*E-mail: palasino@conicet.gov.ar; kardill@usc.edu; jstanbac@usc.edu; paterson@usc.edu; cgalindo@geo.ucm.es; monika.b.leopold@gmail.com

INTRODUCTION

Magmas can experience multiple physical and chemical processes during their residence time within the crust before eruption or solidification into plutons. Particularly, in a thermally mature crust, magmas can be maintained above their solidus for thousands to millions of years and form a complex interconnected network of crystal-melt mixtures which are commonly not in isotopic equilibrium (e.g., Broxton et al., 1989; Christensen et al., 1995; Davidson et al., 2001, 2008; Cooper and Reid, 2003; Costa et al., 2003; Lowery Claiborne et al., 2006; Barbey et al., 2008; Ramos and Reid, 2005; Wallace and Bergantz, 2005; Kaiser et al., 2016; Alasino et al., 2017). This crustal-scale maturity, achieved by episodic intrusions from the lower crust through time (e.g., de Silva et al., 2006; Paterson et al., 2011; Karakas et al., 2017), allows magma chambers to evolve to highly dynamic hydrogranular environments (e.g., Bergantz et al., 2017), in which extensive mixing, mingling, fractionation, recycling, and contamination can modify the original magma source signatures. In this context, physical and chemical instabilities driven by internal thermal, compositional, and rheological gradients can form structural and compositional diversity in chambers by late, local movement of the crystal-rich system (e.g., Weinberg et al., 2001; Paterson et al., 2005, 2016, 2019; Žák and Klomínský, 2007; Vernon and Paterson, 2008; Ruprecht et al., 2008; Bachmann and Bergantz, 2008; Paterson, 2009; Pinotti et al., 2016; Bergantz et al., 2017; Rocher et al., 2018). Deciphering the timing and mechanisms of magmatic structure formation, and how these structures interact with local and regional strain fields, is essential to understand long-lived magmatic systems. This relationship influences our interpretation of chamber construction and evolution and reconstruction of tectonic records.

Mechanical instabilities can occur along internal contacts either between separate magma batches (Bergantz, 2000; Žák and Paterson, 2005; Memeti et al., 2010) or along solidification fronts within magma chambers (Marsh, 1996, 2006; Žák and Paterson, 2010; Rocher et al., 2018). These boundary-layer

instabilities can take different forms depending on the location of the layer and crystal growth in the chamber (e.g., Jaupart and Tait, 1995; Bergantz, 2000). For example, along the horizontal roof of a chamber, magma convection can produce chemical and physical instabilities that cause crystal-rich batches to descend, or "drip", from the roof (e.g., Bergantz and Ni, 1999; Rocher et al., 2018), while at a vertical or sloping margin, convection would generate a sidewall current (e.g., Jaupart and Tait, 1995; Žák and Paterson, 2010; Paterson et al., 2016, 2019). Marsh (1996, 2006, 2013, 2015) examined the growth of solidification fronts in chambers where the cooling is faster at the roof than at deeper levels along walls. He suggested that these fronts may detach from the roof, generating a crystal-rich magma avalanche toward hotter and deeper levels of the chamber (e.g., Žák and Paterson, 2010). Davis et al. (2007) used the concept of transient particle pressure in magma slurries to argue that magmas affected by earthquake activity could partially fluidize crystal mushes in seconds, resulting in an instantaneous decrease in pressure in the melt phase, in situ bubble formation, and thus large-scale destabilization of the mush, similar to the deformation of wet sediments during seismic loading (e.g., Sumita and Manga, 2008). Petford (2009) suggested that excess pressure due to new bubble formation provides a mechanism for promoting chamber-wide instability through overpressurization of the magma.

A field-based example of solidification front instability is found in the Late Cretaceous Sonora Pass Intrusive Suite, Sierra Nevada, California, USA (e.g., Wahrhaftig, 1979; Macias, 1996, Leopold, 2016) (Fig. 1). The oldest unit, the Kinney Lakes granodiorite (KLG), intruded the Bummers Flat granodiorite (BFG) at 95.6 ± 1.5 Ma (Leopold, 2016) and exhibits a ~2 km^2 area of complex schlieren and a range of other magmatic structures along the intrusive contact with the BFG (Fig. 2). This zone is characterized largely by coupled melanocratic (schlieren) and leucocratic mineral layering but also includes blocks of host-rock material, enclave swarms, and magmatic folds and faults (e.g., Leopold, 2016). In this paper, we explore the structure and composition of schlieren in the KLG in the Sonora Pass Intrusive Suite and their significance at the margins of the intrusion. We present the structural features of the study area, focusing on a comprehensive data set of field observations, structural data, whole-rock element geochemistry, and Sr and Nd isotope compositions of the schlieren troughs in the KLG. Our results provide insight into solidification-front instabilities in active magma chambers, where large-scale magma avalanching (10^2–10^3 m wide), caused by large-scale collapse of a crystal-rich magma mush, may be focused along the margin of a magma body.

GEOLOGICAL SETTING

The Sierra Nevada continental arc formed across a transitional oceanic to continental margin and was largely constructed during three Mesozoic arc flareup periods in the Late Triassic, Jurassic, and Cretaceous (Armstrong and Ward, 1993; DeCelles et al., 2009; Paterson and Ducea, 2015; Kirsch et al., 2016) (Fig. 1A). The Late Cretaceous arc flareup was 10^2–10^3 times more voluminous than previous arc flareups (Paterson and Ducea, 2015) and emplaced calc-alkaline tonalite, granodiorite, and granite plutons, which form a large part of the presently exposed Sierra Nevada batholith.

The Sonora Pass region of the Sierra Nevada batholith, between 38°N and 39°N latitude, was initially studied by Slemmons (1953) and was subsequently mapped at a regional scale (Giusso, 1981; John, 1983; Huber, 1983; Wahrhaftig, 2000). The Sonora Pass Intrusive Suite (SPIS) is the northernmost concentrically zoned intrusive complex of the Cretaceous Sierra Nevada batholith (Fig. 1A) (e.g., Bateman, 1992; Macias, 1996; Leopold, 2016). It is also the smallest (~650 km^2) of four Late Cretaceous nested intrusive complexes ~1000 km^2 that intrude along the axis of the Sierra Nevada batholith (Stern et al., 1981; Kistler et al., 1986; Bateman, 1992) (Fig. 1A). The SPIS was emplaced during the peak of the Cretaceous flareup (Paterson and Ducea, 2015; Cao et al., 2015) at pressures between 2.0 and 3.5 ± 0.6 kbar (Macias, 1996).

The SPIS consists of two main intrusive units, the Kinney Lakes hornblende-biotite granodiorite (95.6 ± 1.5 Ma; Leopold, 2016) and the Topaz Lake biotite granodiorite (90.1 ± 1.1 Ma; Leopold, 2016) (Fig. 1B). The SPIS intruded into the Bummers Flat granodiorite (109.8 ± 1.2 Ma; Leopold, 2016) in the west and Paleozoic metasediments in the east. The metasediments have been interpreted to be remnants of the Snow Lake passive-margin block (e.g., Lahren and Schweickert, 1989; Memeti et al., 2010). To the south, the SPIS intrudes Jurassic mafic to ultramafic plutonic rocks and Cretaceous metavolcanic units (Lahren et al., 1990; John et al., 1994; Cao et al. 2015). The SPIS is compositionally normally zoned, with a felsic, porphyritic core (Topaz Lake granodiorite) intruding the less differentiated, equigranular Kinney Lakes granodiorite (Macias, 1996; Leopold, 2016). Contacts between the two units are generally subvertical (Macias, 1996; Leopold, 2016). Initial $^{87}Sr/^{86}Sr_i$ ratios between 0.7055 and 0.7058 within the SPIS indicates that the two units are isotopically similar (Macias, 1996).

The study area is located in the southwestern part of the SPIS (Fig. 1B) at the intrusive margin between the KLG and BFG units. A region of concentrated magmatic structures and complex schlieren is exposed here, which has been interpreted to have formed from late-stage magmatic flow (Leopold, 2016).

METHODS

Forty-two (42) samples were collected for petrography. One granodiorite sample of KLG, one leucogranite sample of KLG, three schlieren samples in the KLG unit, and three samples of felsic layers found between sampled schlieren (herein termed leucocratic bands; see Table 1) were selected for whole-rock major- and trace-element analyses using inductively coupled plasma–mass spectrometry (ICP-MS) at Activation Laboratories, Ancaster, Ontario, Canada, under the "4LithoResearch" package, following the procedure described at http://www.actlabs.com (Table 2). Leucocratic band and schlieren samples

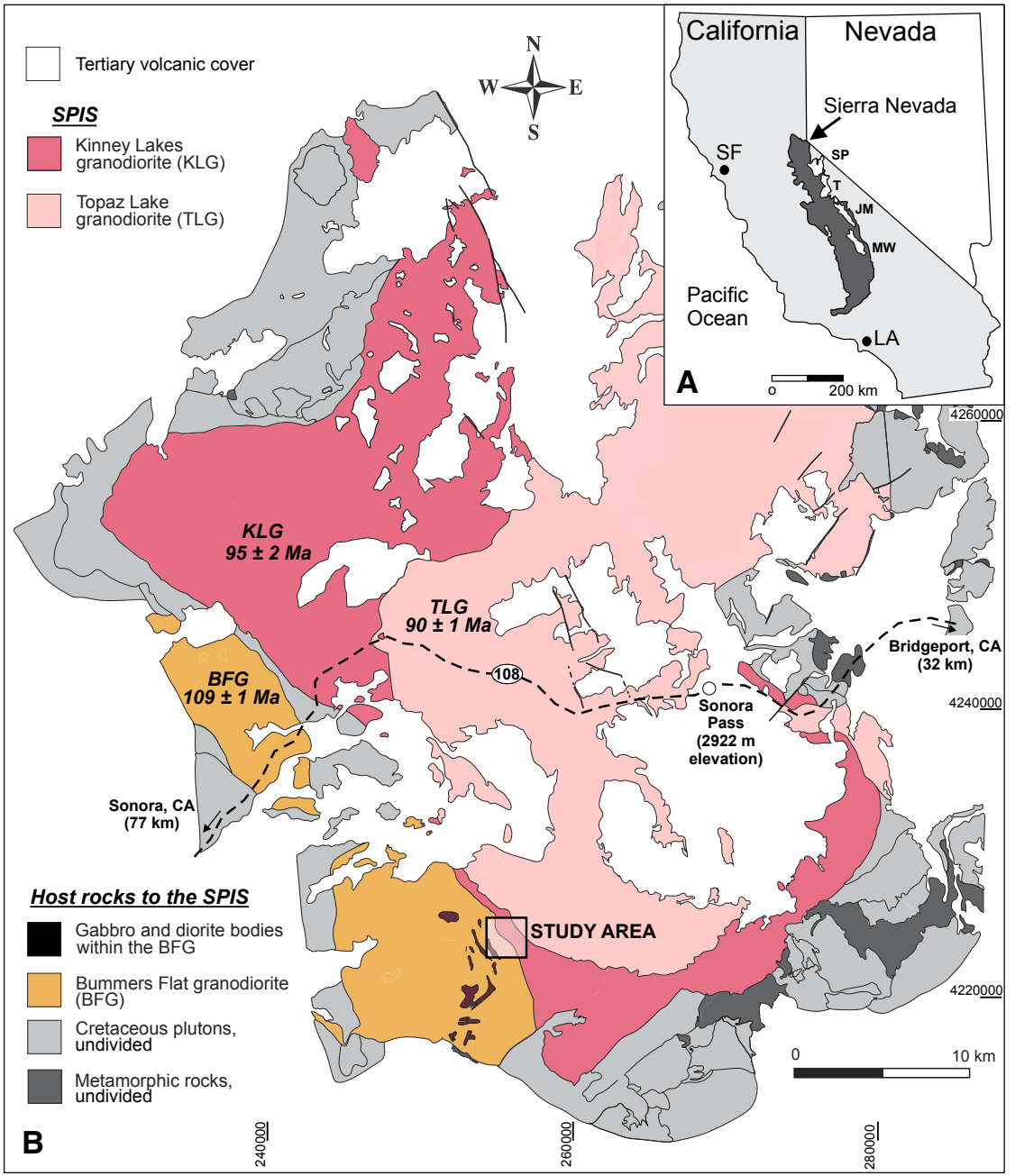

Figure 1. Simplified regional geological map of the Sonora Pass Intrusive Suite. (A) Location of the Sierra Nevada arc section in dark gray, and the study area, labeled SP. T—Tuolumne Intrusive Suite; JM—John Muir Intrusive Suite; MW—Mount Whitney Intrusive Suite; SF—San Francisco; LA—Los Angeles. (B) Map of the main plutonic units of the Sonora Pass Intrusive suite (SPIS) and plutonic host rocks relevant to this study. Box shows the location of this study (see Fig. 2). Geologic map of the Sonora Pass Intrusive Suite is simplified from John (1983) and unpublished mapping (D.A. John, 2015, personal commun.). U-Pb zircon ages shown are from Leopold (2016). Coordinate system is Universal Transverse Mercator zone 11S (in meters), North American Datum 1983. CA—California.

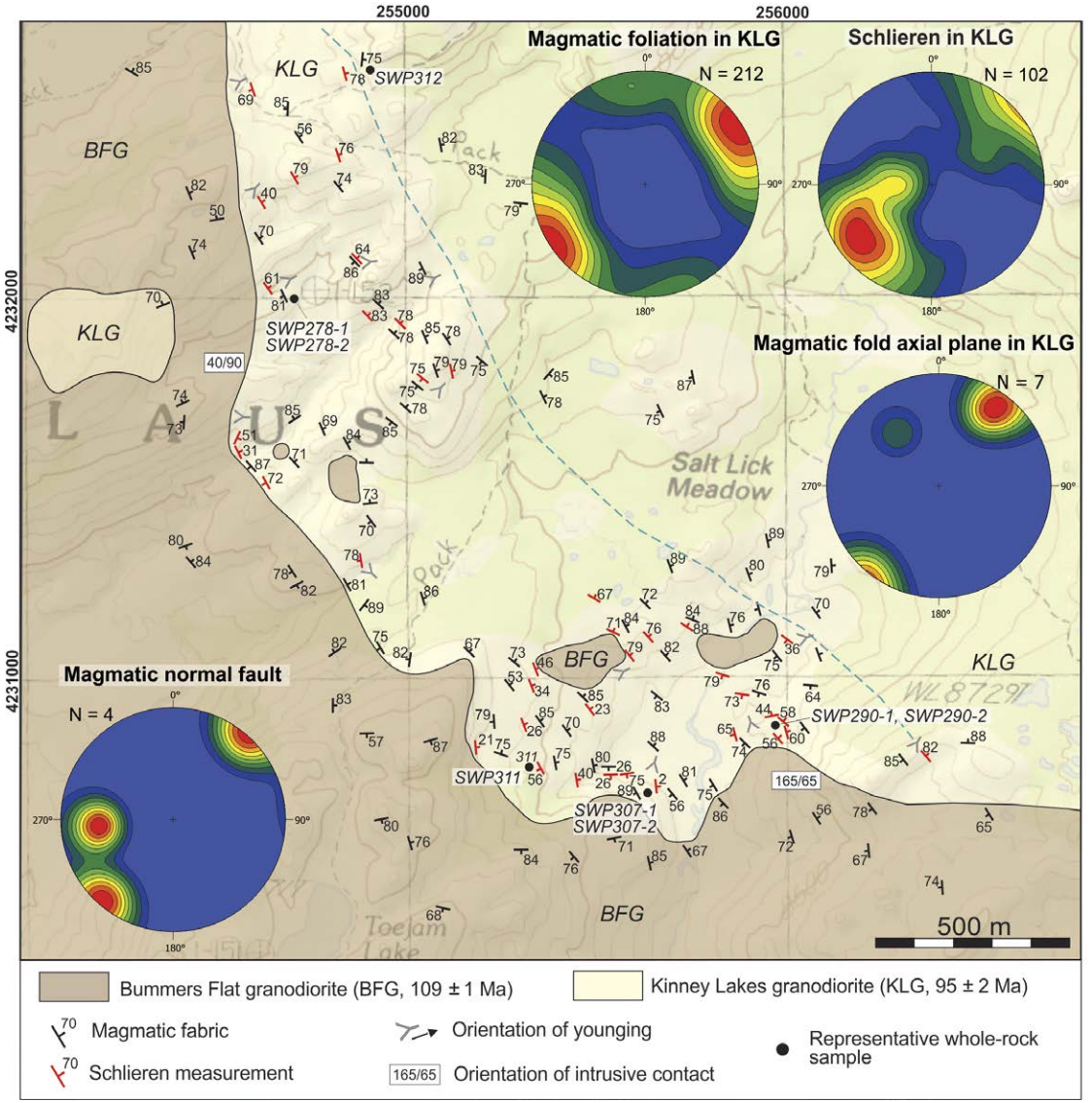

Figure 2. Geologic map of the southwestern intrusive contact of the Kinney Lakes granodiorite (KLG) with the Bummers Flat granodiorite (BFG). Map shows representative structural data from both igneous units. Multiple magmatic foliations are recognized. Structural data in black correspond to the regional magmatic foliations; structural data in red correspond to the orientation of the schlieren. Blue line delineates the extent of the schlieren zone found at the margin. Local younging direction determined from graded layers and trough cut-offs is also shown; the arrowhead indicates its sense. The strike/dip (in degrees) used for the orientation of intrusive contact is according to the right-hand rule. Stereonets (equal-area, lower-hemisphere projections) show poles to planes of magmatic structures, such as regional magmatic foliations, schlieren orientation, and magmatic folds and faults in the KLG. Coordinate system is Universal Transverse Mercator zone 11S (in meters), North American Datum 1983.

TABLE 1. SUMMARY OF PETROGRAPHIC OBSERVATIONS OF SOME REPRESENTATIVE SAMPLES WITH GEOCHEMICAL DATA, SONORA PASS INTRUSIVE SUITE

Sample	Rock type	Mineralogy	Observations
SWP312	Granodiorite	Pl > Qtz > Hbl-Bt > Kfs > Spn > Opq > Ap > Zrn	
SWP278-2	Schlieren	Hbl > Bt > Opq > Spn > Pl > Qtz > Ap > Zrn	K-feldspar is rare
SWP290-1	Schlieren	Hbl > Bt > Opq > Pl > Spn > Qtz > Ap > Zrn	Fine-grained quartz; K-feldspar is rare
SWP307-1	Schlieren	Bt > Hbl > Spn > Opq > Pl > Qtz > Ap > Zrn	Fine-grained quartz; K-feldspar is rare
SWP278-3	Leucocratic band	Pl-Qtz > Kfs > Hbl-Bt > Opq-Spn > Ap > Zrn	
SWP290-2	Leucocratic band	Pl > Qtz > Kfs > Bt > Hbl > Spn > Opq > Ap > Zrn	
SWP307-2	Leucocratic band	Pl > Qtz > Kfs > Bt > Hbl > Opq > Spn > Ap > Zrn	Secondary muscovite
SWP311	Leucogranodiorite	Pl > Qtz-Kfs > Bt	Hornblende and accessories are rare; secondary muscovite

Abbreviations: Pl—plagioclase; Qtz—quartz; Hbl—hornblende; Bt—biotite; Kfs—K-feldspar; Spn—sphene; Opq—opaques; Ap—apatite; Zrn—zircon.

were paired, i.e., they were collected from the same locality and are in contact. Two additional samples of KLG were sampled by J. Miller (personal commun., 2018) and analyzed using X-ray fluorescence at Pomona College, Claremont, California (see Lackey et al. [2012] for further details regarding X-ray fluorescence analysis), for whole-rock major elements, and for trace elements in the same samples at the Washington State University GeoAnalytical Lab, Pullman, Washington, USA, using ICP-MS following the procedure described at https://environment.wsu.edu/facilities/geoanalytical-lab/technical-notes/icp-ms-method/. Additionally, six representative igneous samples of nearby units from this work and that of J. Miller (personal commun., 2018) (two mafic samples and two granodiorite samples of the BFG, and two granodiorite samples of the Topaz Lake granodiorite unit) were selected for major- and trace-element analysis. Nineteen (19) samples of the SPIS from Macias (1996) are also included for comparison.

Strontium (Sr) and neodymium (Nd) isotopic analyses of six representative KLG samples (one granodiorite, one leucogranite, two felsic layers, and two schlieren) were carried out at the Geochronology and Isotope Geochemistry Centre of Complutense University, Madrid, Spain (Table 3). Whole-rock powders were decomposed in 4 ml HF and 2 ml HNO_3 in Teflon digestion bombs heated for 48 h at 120 °C and finally in 6 M HCl. Samarium (Sm) and Nd were determined by isotope dilution using spikes enriched in ^{149}Sm and ^{150}Nd. Ion exchange techniques were used to separate the elements for isotopic analysis. Sr and rare earth elements (REEs) were separated using Bio-Rad AG50 × 12 cation exchange resin. Sm and Nd were further separated from the REE group using Bio-Beads coated with 10% HDEHP [Di-(2-ethylhexyl) phosphoric acid]. Isotopic analyses were made on an automated multicollector VG SECTOR 54 mass spectrometer. Analytical uncertainties are estimated to be 0.006% for $^{143}Nd/^{144}Nd$ and 0.1% for $^{147}Sm/^{144}Nd$. Replicate analyses of the JNdi Nd-isotope standard yielded an average $^{143}Nd/^{144}Nd$ ratio of 0.512106 ± 0.000005 (2σ) with n = 7 (accepted value 0.512115 ± 0.000002; Tanaka et al., 2000), and the NBS-987 Sr-isotope standard yielded an average $^{87}Sr/^{86}Sr$ ratio of 0.710248 ± 0.000019 (2σ) with n = 12. Errors are quoted throughout as two standard deviations from measured or calculated values.

FIELD AND STRUCTURAL RELATIONSHIPS AT THE KINNEY LAKES GRANODIORITE MARGIN

Intrusive Contact between the Kinney Lakes Granodiorite and Bummers Flat Host Rock

The southwestern intrusive contact between the BFG and the KLG is relatively straight in the northern part of the study area, with a general NNW-SSE–trending strike, but is highly irregular (at the 100 m scale) in the south, where the contact strikes east-west (Fig. 2). The contact between the KLG and the BFG is highly discordant. It varies from moderately dipping (~60° NE) to vertical along strike, truncating all structures in the BFG. Several pegmatites and aplite dikes (up to 1 m wide) from the KLG intrude the BFG. The KLG also formed a small cupola (0.1 km^2) in the BFG (Fig. 2). Local (centimeter to decimeter scale) solid-state shears are found in the BFG close to the margins of the KLG. No solid-state deformation was found in the KLG within the study area, although it is reported further to the east, near the contact with metasedimentary host rocks and older mafic plutons (Leopold, 2016).

A rich array of magmatic structures is recognized at the margin of the KLG. These include: regional and local magmatic fabrics, schlieren and trough structures, mafic magmatic enclaves, leucogranite and mafic dikes, magma mingling zones, host-rock xenoliths (of BFG), cognate inclusions (of earlier, recycled KLG), and magmatic faults and folds. The zone of highly concentrated magmatic structures extends ~800 m from the BFG-KLG contact to the blue dashed line in Figure 2 and is discussed in detail below.

Regional Magmatic Fabrics

The dominant regional magmatic fabric in the KLG is NW-SE–striking and steeply dipping to subvertical (60°–90°). The average orientation in the study area is 154/90 (strike/dip according to the right-hand rule) (Fig. 2; n = 130 measurements). It is defined by aligned hornblende, biotite, and plagioclase.

TABLE 2. MAJOR- AND TRACE-ELEMENT COMPOSITIONS OF THE IGNEOUS SAMPLES

	Host rock				Sonora Pass Intrusive Suite										
Unit	BFG	BFG	BFG	BFG	KLG	KLG	KLG	KLG	KLG	KLG	KLG	KLG	KLG	KLG	KLG
Sample	SWP272*	SWP272-2*	SWP279-2*	SICN3†	SWP312*	SICN17†	SICN25†	S14-6§	S10-2§	S72-3§	S72-4§	S52-2§	S22-8§	R52-9§	S28-8§
Major elements (wt%)															
SiO_2	48.34	43.71	67.06	67.59	67.16	66.14	64.98	61.2	65.4	65.2	66.6	64	67.7	64.9	68
TiO_2	1.68	1.08	0.51	0.36	0.52	0.56	0.55	0.80	0.57	0.56	0.63	0.63	0.48	0.55	0.44
Al_2O_3	17.96	14.03	15.51	14.66	15.81	15.49	15.66	17.2	15.6	15.7	15.7	16.3	15.1	15.8	15.2
FeO^t	10.82	13.71	4.81	3.01	3.26	4.31	4.26	6.25	4.46	4.99	4.22	5.37	3.99	4.51	3.90
MgO	7.43	12.99	1.54	0.96	1.14	1.64	1.53	2.59	1.40	1.94	1.54	2.19	1.46	1.78	1.38
MnO	0.17	0.18	0.09	0.06	0.06	0.07	0.06	0.09	0.07	0.08	0.06	0.09	0.06	0.07	0.07
CaO	9.14	9.03	3.72	2.75	3.60	4.06	3.91	5.55	3.99	4.14	3.95	4.56	3.54	4.11	3.29
Na_2O	3.18	1.49	3.49	3.32	3.63	3.32	3.36	3.73	3.80	3.38	3.67	3.51	3.33	3.67	3.47
K_2O	1.18	2.35	2.22	3.31	3.21	3.01	3.41	1.98	2.67	2.89	3.13	2.73	3.46	2.85	3.35
P_2O_5	0.1	0.06	0.11	0.1	0.13	0.16	0.15	0.21	0.16	0.16	0.16	0.16	0.12	0.16	0.12
LOI (%)	1.48	1.95	0.85	—	0.46	—	—	0.55	1.80	0.75	0.55	0.45	0.25	0.45	0.65
Trace elements (ppm)															
Cs	5.3	20.5	2.1	3.9	1.6	5.6	4.2	—	—	—	—	—	—	—	—
Rb	53	108	87	115	95	85.1	94.7	69.3	94.2	105	104	107	131	92.1	118
Sr	754	478	374	406	496	519	572	641	562	451	543	517	431	504	426
Ba	244	275	859	1462	674	938	1141	790	823	791	649	753	784	856	679
La	10.8	7.47	32.2	35.6	21.7	15.2	21.1	27.2	23.2	27.2	22.3	23.1	22.1	25.8	19.2
Ce	24.7	18	57.9	69.4	34.7	34.5	41.2	55.6	41.7	49.5	41.0	47.3	46.0	44.7	32.2
Pr	3.39	2.49	6.36	4.9	3.63	7	5.1	6.46	4.66	5.51	4.67	5.58	5.25	4.97	3.48
Nd	15.1	10.9	22.3	20.1	13.4	13.3	19	24.8	17.7	20.7	17.9	20.5	19.4	18.4	12.9
Sm	3.73	2.8	4.13	3.3	2.44	1.6	3.4	4.43	3.13	3.63	3.17	3.80	3.34	3.25	2.29
Eu	1.18	1.02	0.84	—	0.66	—	—	1.15	0.82	0.87	0.85	0.95	0.83	0.87	0.62
Gd	3.52	2.77	3.28	—	1.79	—	—	3.76	2.50	3.16	2.58	3.25	2.78	2.75	1.90
Tb	0.55	0.4	0.5	—	0.24	—	—	0.51	0.32	0.44	0.33	0.47	0.38	0.36	0.25
Dy	3.17	2.36	2.88	—	1.31	—	—	2.71	1.58	2.49	1.59	2.64	2.05	1.89	1.29
Ho	0.59	0.43	0.56	—	0.23	—	—	0.50	0.28	0.49	0.29	0.52	0.39	0.35	0.24
Er	1.63	1.15	1.73	—	0.63	—	—	1.31	0.76	1.36	0.74	1.43	1.08	0.92	0.64
Tm	0.21	0.15	0.26	—	0.09	—	—	0.19	0.10	0.20	0.10	0.22	0.16	0.13	0.09
Yb	1.29	0.92	1.7	—	0.55	—	—	1.15	0.64	1.30	0.65	1.36	1.04	0.82	0.58
Lu	0.18	0.13	0.26	—	0.08	—	—	0.17	0.10	0.20	0.10	0.20	0.16	0.13	0.09
U	0.9	0.74	3.45	0.5	3.55	1.4	0.2	2.90	4.38	4.10	3.57	3.96	6.41	3.72	4.64
Th	2	0.94	15.8	11.2	10.8	5.2	3.7	11.3	11.8	16.4	12.7	11.2	15.2	17.8	23.0
Y	17.1	12.2	17.8	11.5	6.7	11.2	9.9	—	—	—	—	—	—	—	—
Nb	3.6	1.2	7.9	9.5	2.2	8	7.4	10.8	7.93	10.4	8.72	10.2	10.7	8.96	8.68
Zr	72	45	153	134	99	122	101	150	124	146	105	133	112	117	108
Hf	1.9	1.3	3.9	4.6	2.6	3.2	2.8	—	—	—	—	—	—	—	—
Ta	0.34	0.14	1.08	1.3	0.47	4.9	2.4	—	—	—	—	—	—	—	—
Ga	17	15	17	16.3	18	18.1	17.4	—	—	—	—	—	—	—	—
Sc	43	21	8	5.9	4	9.1	8.8	—	—	—	—	—	—	—	—

Notes: Total iron expressed as FeO^{total}. Dashes indicate no value given (not analyzed). BFG—Bummers Flat granodiorite; KLG—Kinney Lakes granodiorite; SCH—schlieren in KLG; LB—leucocratic band in KLG; Lg—leucogranite in KLG; TLG—Topaz Lake granodiorite; LOI—loss on ignition.

*Samples from this work.

†Samples from J. Miller, personal commun., 2018.

§Samples from Macias (1996).

(*continued*)

TABLE 2. MAJOR- AND TRACE-ELEMENT COMPOSITIONS OF THE IGNEOUS SAMPLES (*continued*)

	Sonora Pass Intrusive Suite														
Unit	KLG	SCH	SCH	SCH	LB	LB	LB	Lg	TLG	TLG	TLG	TLG	TLG	TLG	TLG
Sample	R48-9§	SWP278-2*	SWP290-1*	SWP307-1*	SWP278-3*	SWP290-2*	SWP307-2*	SWP311*	SICN10†	SICN12†	S50-4§	S68-4§	S60-4§	S24-6§	S103-4§
Major elements (wt%)															
SiO_2	65.7	54.25	53.95	61.51	65.91	69.46	67.3	73.49	68.67	68.32	67.6	67	67.7	68.1	68.5
TiO_2	0.65	1.62	1.79	1.21	0.37	0.55	0.49	0.13	0.46	0.45	0.44	0.46	0.41	0.41	0.32
Al_2O_3	15.9	14.78	12.52	13.1	16.48	14.45	16.09	14.95	15.66	15.73	16	15.6	16	15.2	15.5
FeO^t	4.44	10.59	12.73	8.11	3.2	3.81	3.52	1.25	2.95	3.04	3.38	3.35	3.28	3.17	2.37
MgO	1.58	4.73	4.87	3.32	1.07	1.32	1.3	0.31	0.05	0.05	1.01	1.16	1.06	0.88	0.61
MnO	0.06	0.21	0.25	0.16	0.05	0.07	0.07	0.03	2.66	2.74	0.05	0.06	0.05	0.05	0.05
CaO	4.01	6.22	4.95	3.91	4.57	2.96	3.34	1.75	0.89	0.94	3.39	3.3	3.48	2.97	2.46
Na_2O	3.78	2.96	2.15	2.71	3.9	2.97	3.74	3.10	3.15	2.91	4.24	4.08	4.27	4.05	4.07
K_2O	2.91	2.78	3.7	3.95	2.47	4.14	3.32	4.59	3.87	3.79	2.91	3.08	2.9	3.28	4.05
P_2O_5	0.18	0.42	0.43	0.26	0.13	0.12	0.11	0.03	3.68	4.07	0.16	0.14	0.15	0.15	0.13
LOI (%)	0.3	—	—	0.73	0.48	0.48	0.79	0.39	0.15	0.15	1.05	0.5	0.5	0.8	0.5
Trace elements (ppm)															
Cs	—	2.3	4.2	3.3	1.3	2	2	2.3	6	7	—	—	—	—	—
Rb	101	102	154	136	53	106	89	127	122	134	133	115	117	132	149
Sr	563	368	212	222	579	357	357	249	563	578	615	557	614	507	566
Ba	827	621	488	438	916	671	423	415	744	1227	704	736	742	675	1133
La	24.6	55.6	129	60.4	16.5	37.6	33.4	17.3	24.2	16.1	25.5	18.8	20.9	28.2	32.2
Ce	44.8	142	227	115	34.3	62.4	52.6	21.4	49.9	35.1	47.2	33.6	38.9	48.4	51.8
Pr	5.05	17.4	22.4	12.4	3.92	6.04	5.13	1.66	5.9	7.1	5.21	3.78	4.36	5.30	5.57
Nd	19.4	67.4	79.9	43.6	14.6	20.6	16.8	4.73	16.5	13.1	18.6	13.8	15.6	19.2	19.8
Sm	3.44	13	13.9	8.28	2.61	3.52	2.93	0.7	3.5	3.1	3.12	2.42	2.67	3.13	3.10
Eu	0.93	2.68	2.59	1.63	0.73	0.82	0.76	0.26	—	—	0.78	0.65	0.72	0.75	0.73
Gd	2.76	9.8	10.3	6.34	1.96	2.62	2.18	0.57	—	—	2.39	1.87	2.08	2.45	2.25
Tb	0.34	1.37	1.44	0.89	0.3	0.36	0.31	0.09	—	—	0.29	0.23	0.25	0.30	0.27
Dy	1.69	7.52	7.93	4.93	1.52	2.05	1.73	0.49	—	—	1.44	1.12	1.26	1.49	1.33
Ho	0.30	1.39	1.46	0.93	0.28	0.39	0.32	0.1	—	—	0.27	0.20	0.23	0.28	0.24
Er	0.77	3.71	4.21	2.53	0.82	1.12	0.91	0.29	—	—	0.75	0.52	0.63	0.77	0.67
Tm	0.11	0.56	0.62	0.374	0.119	0.16	0.148	0.05	—	—	0.11	0.07	0.09	0.11	0.10
Yb	0.65	3.47	4.02	2.51	0.78	1.09	1.01	0.37	—	—	0.70	0.46	0.58	0.73	0.66
Lu	0.10	0.54	0.64	0.393	0.112	0.165	0.164	0.06	—	—	0.10	0.07	0.09	0.11	0.10
U	3.97	5.38	8.75	8.39	1.6	3.99	7.37	3.44	4.3	6.6	7.27	4.53	3.66	5.40	4.05
Th	12.1	18.3	78.6	50.2	4.54	32.8	33	22.1	12.7	11.9	13.42	10.72	10.39	7.76	14.89
Y	—	43.2	46.4	28.1	8.9	12	10.2	3.1	8.5	8.5	—	—	—	—	—
Nb	9.26	20.1	26	16.1	2.7	5	4.6	<0.2	8.9	7.3	8.43	6.93	8.20	9.68	9.36
Zr	123	324	405	268	94	117	118	54	110	98.8	127	106	105	122	120
Hf	—	7.8	10.4	7.1	2.3	2.9	3.1	1.6	3.5	2.8	—	—	—	—	—
Ta	—	3	3.64	2.16	0.64	0.94	0.82	0.21	3.4	5.1	—	—	—	—	—
Ga	—	22	23	19	17	15	17	13	20.1	20.3	—	—	—	—	—
Sc	—	20	23	15	5	5	5	1	5.6	7.1	—	—	—	—	—

(*continued*)

TABLE 2. MAJOR- AND TRACE-ELEMENT COMPOSITIONS OF THE IGNEOUS SAMPLES (*continued*)

	Sonora Pass Intrusive Suite				
Unit	TLG	TLG	TLG	TLG	TLG
Sample	S69-6§	S102-4§	S118-4§	S124-4§	S48-9§
Major elements (wt%)					
SiO_2	68.2	71.5	71	70.9	68.5
TiO_2	0.49	0.25	0.26	0.31	0.36
Al_2O_3	15.4	14.3	15.3	15	15.2
FeO^t	3.64	2.11	2.03	2.46	2.88
MgO	1.19	0.51	0.48	0.61	0.65
MnO	0.06	0.04	0.04	0.05	0.06
CaO	3.55	1.9	2.11	2.46	2.64
Na_2O	3.96	4.01	4.01	4.13	4.33
K_2O	2.58	3.56	3.99	3.26	3.22
P_2O_5	0.17	0.09	0.09	0.13	0.14
LOI (%)	0.7	0.65	0.55	0.45	1
Trace elements (ppm)					
Cs	—	—	—	—	—
Rb	101	162	166	160	141
Sr	578	408	500	512	570
Ba	497	670	1149	125	675
La	26.6	25.8	24.0	—	29.2
Ce	45.0	44.3	42.3	—	49.6
Pr	4.95	4.84	4.60	—	5.28
Nd	18.7	16.2	16.4	—	18.3
Sm	3.05	2.61	2.67	—	2.95
Eu	0.76	0.58	0.63	—	0.71
Gd	2.45	1.96	1.90	—	2.26
Tb	0.30	0.25	0.23	—	0.27
Dy	1.47	1.25	1.13	—	1.34
Ho	0.27	0.24	0.21	—	0.25
Er	0.71	0.70	0.60	—	0.68
Tm	0.10	0.11	0.09	—	0.10
Yb	0.65	0.75	0.59	—	0.68
Lu	0.10	0.12	0.09	—	0.10
U	4.82	2.70	3.47	—	6.20
Th	14.9	17.8	18.9	—	18.9
Y	—	—	—	—	—
Nb	8.53	9.69	8.67	—	9.41
Zr	122	113	103	—	133
Hf	—	—	—	—	—
Ta	—	—	—	—	—
Ga	—	—	—	—	—
Sc	—	—	—	—	—

A second magmatic fabric of equal intensity but unevenly distributed in the study area, also defined by hornblende and biotite, is ENE striking and is also steeply dipping to subvertical (average orientation 078/86; $n = 82$ measurements; Fig. 2). Lineation plunges defined by hornblende are steep to subvertical (Leopold, 2016). Relative timing relationships between the two fabrics are unclear and, in many cases, contradictory. These two fabrics are widespread across the KLG unit (Macias, 1996; Leopold, 2016).

Compositionally Defined Layering and Structures

Planar Schlieren and Trough Structures

The most common type of compositional layering observed within the KLG consists of alternating schlieren and leucocratic bands (or felsic schlieren) that form planar to trough-like geometries (Figs. 3A–3D). Layer thickness is on the order of centimeters to meters. Schlieren consist of medium-grained ferromagnesian minerals hornblende and biotite, zircon, sphene, apatite, and opaque minerals, ± quartz and plagioclase (Fig. 3A; Table 1). Leucocratic bands between schlieren contain abundant coarse-grained feldspar (plagioclase dominates over microcline) + quartz with minor ferromagnesian and accessory minerals (Table 1). Commonly, schlieren have a basal surface with a sharp contact defined by a thin, densely packed layer of mafic minerals (<1 cm), whereas the upper contact is commonly less well defined and gradational into the leucocratic bands at the centimeter scale (Figs. 3A, 4, 5).

At the map scale, schlieren broadly strike margin parallel, with an approximately NNW-SSE orientation in the north of the study area. However, orientations are highly variable at the outcrop scale (Fig. 2). There is no map-scale schlieren alignment in the southern part of the study area. Schlieren dips range widely from 2° to 88° but are on average steeply dipping to subvertical toward the SW and NE (Fig. 2). The steepest dips are mainly found near the NNW-SSE–striking contact, while shallow dips are dominant near the east-west–striking contact (Fig. 2).

Locally, alternating schlieren and leucocratic bands contain two mineral orientations: the dominant fabric is defined by mafic minerals located in the schlieren aligned parallel to the base of the layer, and the second, less intense fabric of similar strike but with a steeper dip preferentially forms in the leucocratic band. In some places, the NW-striking regional magmatic fabric overprints the schlieren (Fig. 4). Magmatic mineral lineations in the schlieren, defined by hornblende and sphene, are approximately downdip with a tendency to plunge toward the northeast.

Local younging directions are determined from trough cross-cutting relationships, comparable with those found in sedimentary layered rocks (e.g., Weinberg et al., 2001; Paterson, 2009; Figs. 3B, 3D, 4), as well as mineral size and density grading in planar schlieren (Figs. 3A, 4, 5). Together these structures indicate younging to the northeast (mean vector 048), toward the interior of the KLG (Figs. 2, 4, 5).

TABLE 3. Rb-Sr AND Sm-Nd DATA FOR IGNEOUS SAMPLES FROM THE SONORA PASS INTRUSIVE SUITE

Sample	Rb (ppm)	Sr (ppm)	$^{87}Rb/^{86}Sr$	$^{87}Sr/^{86}Sr$	$^{87}Sr/^{86}Sr_t$*	Sm (ppm)	Nd (ppm)	$^{147}Sm/^{144}Nd$	$^{143}Nd/^{144}Nd$	$^{143}Nd/^{144}Nd_t$	$\varepsilon_{Nd(t)}$†
Kinney Lakes granodiorite											
SWP312	95	496	0.550	0.70648	0.70573	2.44	13.4	0.1101	0.51245	0.51238	–2.60
Schlieren in Kinney Lakes granodiorite											
SWP290-1	154	212	2.101	0.70851	0.70567	13.9	79.9	0.1052	0.51242	0.51235	–3.09
SWP307-1	136	222	1.772	0.70817	0.70578	8.28	43.6	0.1148	0.51242	0.51235	–3.14
Leucocratic band in Kinney Lakes granodiorite											
SWP290-2	106	357	0.859	0.70696	0.70580	3.52	20.6	0.1033	0.51242	0.51236	–3.04
SWP307-2	89	357	0.721	0.70679	0.70582	2.93	16.8	0.1054	0.51242	0.51235	–3.11
Leucogranite in Kinney Lakes granodiorite											
SWP311	127	249	1.475	0.70802	0.70603	0.70	4.73	0.0895	0.51243	0.51237	–2.84

Note: The decay constants used in the calculations are the values $\lambda^{87}Rb = 1.42 \times 10^{-11}$ and $\lambda^{147}Sm = 6.54 \times 10^{-12}$ yr^{-1} recommended by the International Union of Geological Sciences (IUGS) Subcommission on Geochronology (Steiger and Jäger, 1977).

*t—time used for the calculation of the isotopic initial ratios; t = 95 Ma.

†Epsilon-Nd values were calculated relative to a present-day chondrite $(^{143}Nd/^{144}Nd)^{today}_{CHUR} = 0.512638$; $(^{143}Sm/^{144}Nd)^{today}_{CHUR} = 0.1967$, where CHUR is chondritic uniform reservoir.

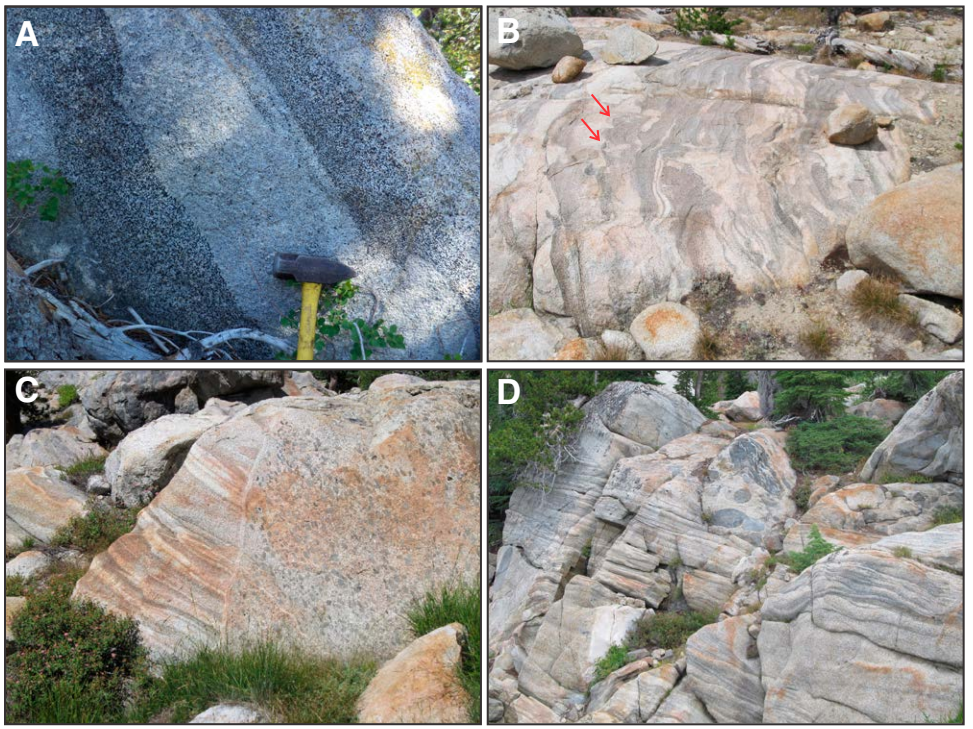

Figure 3. Field photos within the schlieren zone showing typical texture, magma mingling, and typical truncation features with enclave swarms. (A) Close-up view of melanocratic and leucocratic layers with a sharp contact at the base of the schlieren and eastward grading (right-hand side of the photo). (B) Schlieren layering, in places graded, re-intruded by leucogranite and dikes of Kinney Lakes granodiorite (KLG). The package is gently folded. Load-cast features are shown by red arrows. The width of outcrop in the photo is ~4 m. (C) Steep truncation surface of shallowly dipping schlieren by an enclave-rich unit. Height of outcrop in photo is ~2 m. (D) Enclave-rich unit truncating, along a magmatic angular unconformity, shallowly dipping troughs and planar schlieren (some truncation surfaces are evident at the lower right of the image) formed at the Bummers Flat granodiorite–KLG contact. An enclave-rich zone below the schlieren package represents a separate magma batch from the upper unit. Height of outcrop in photo is ~3 m.

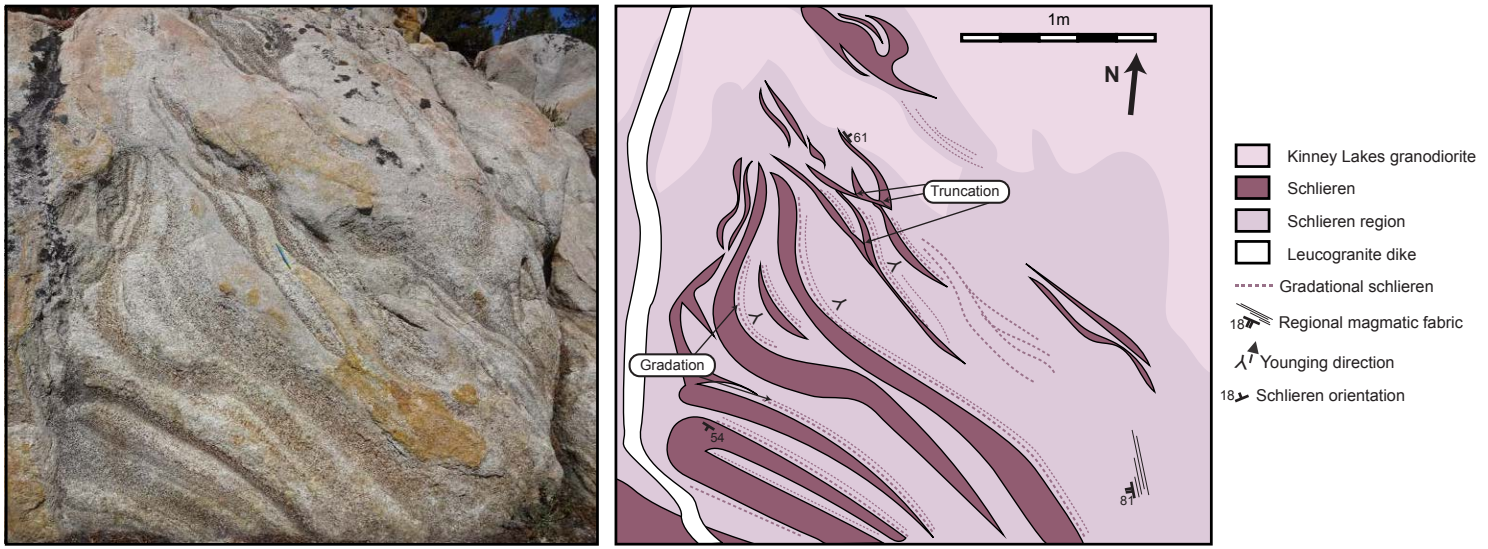

Figure 4. Sloped outcrop facing north (dip toward viewer) of a package of truncated schlieren troughs indicating an orientation of younging toward the northeast in the Kinney Lakes granodiorite margin. Schlieren dip increases toward the northeast. Coarse schlieren troughs show mineral size grading, indicating consistent younging toward the northeast. Some schlieren in the southwestern corner of the photo are magmatically folded. The regional fabric is well-defined SE-NW striking (164/81, right-hand rule). At left of the photo, a leucogranite dike truncates the schlieren packages.

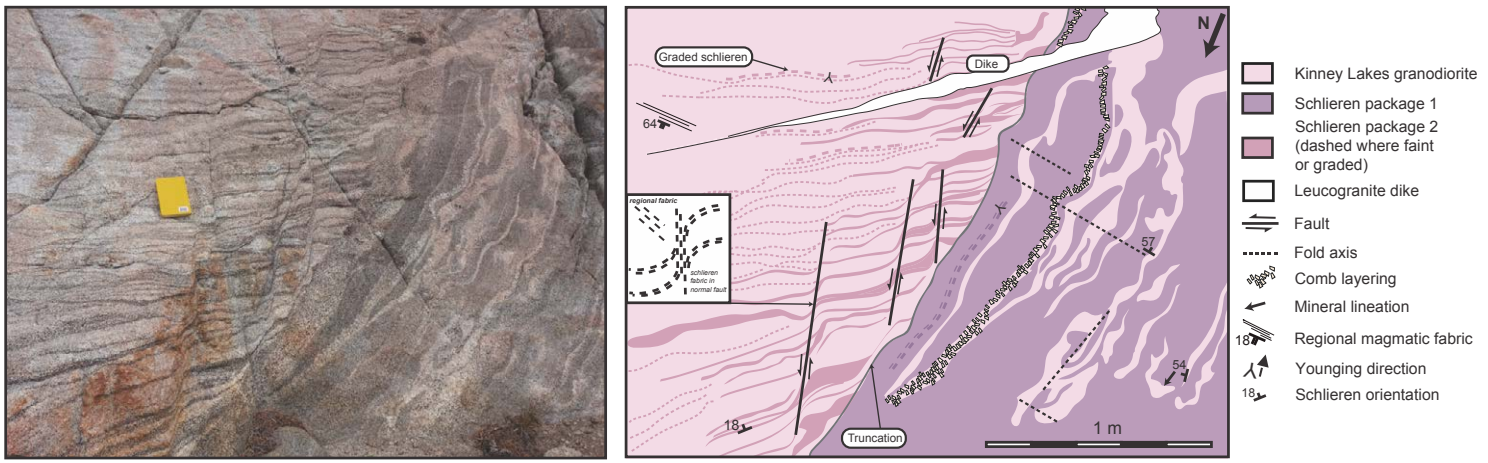

Figure 5. Sloped outcrop facing south (dip toward viewer) of sharply truncated schlieren packages in the Kinney Lakes granodiorite (KLG) margin. The dominant regional magmatic fabric is approximately east-west (e.g., 270/64, right-hand rule). In some places, the regional fabric overprints the fabric in the schlieren packages. On the right-hand (western) side of the outcrop is a schlieren-rich area. Note that the right package truncates the left package and is thus younger. The late dike also supports this because it originates in the right package, drained from KLG magma, and intrudes the left. Layering strikes roughly north-south and is moderately to steeply dipping (351/54). Textural features include comb layering and gradational layering. Magmatic mineral lineation in the schlieren plane defined by hornblende and sphene are approximately down dip, with a tendency toward the NE (54/027; plunge trend). Graded schlieren layers young eastwards in the right-hand-side (western) package, toward the truncation boundary, and most layers have been magmatically folded (axial plane: 085/57), with some layers being folded by multiple events. The left-hand-side (eastern) package has east-west–striking, shallowly dipping schlieren layers (060/18), which are gradually more diffuse eastwards. Top-to-the-west normal faulting is observed close to the moderately dipping truncation boundary. At the faults, magmatic fabric defined by hornblende and biotite is deflected into the fault plane. Schlieren grading suggests that schlieren layers young upwards (and to the south).

Mafic Enclaves

Magmatic mafic enclaves are common within the schlieren zone. Enclaves are up to 20 cm length in the long axis, are rarely contained in the basal sections of schlieren bands, and are more commonly found within meter-scale enclave-rich zones, or enclave swarms (Figs. 3C, 3D, 6A, 6B). In many cases, enclave swarms also contain crystal clots of hornblende and biotite (Fig. 6B).

Two types of enclaves are distinguished at the KLG margin: type 1 has an aphanitic texture, while type 2 contains millimeter-sized feldspar phenocrysts, forming a porphyritic texture. Enclaves locally have felsic rims, or schlieren rims, but more commonly are in direct contact with the host magma.

Within enclave swarms, enclaves may have almost all geometries and sizes: spherical to ellipsoidal, angular to rounded, and quadruple pronged (all seen at a single outcrop: Figs. 3D, 6B). In most enclave swarms, the enclaves appear to have no preferred orientation (Fig. 6B), with some exceptions (Fig. 6A). Where found in isolation, enclaves commonly appear lenticular to elongate parallel with the regional fabric (e.g., Fig. 7A; $n = 17$ enclave long-axis measurements).

Dikes and Small Granitic Bodies

Fine-grained leucogranite bodies and dikes intrude the KLG (Figs. 3B, 3C, 4, 5, 6C). They are dominated by quartz and feldspar, with approximate widths between 10 cm and 5 m and lengths >5 m. Dikes are found in all orientations, but a limited number of measurements show a weak preference for dikes striking NW-SE (average 334/82; $n = 10$). Dikes are usually straight, but are also found folded or faulted, particularly where associated with schlieren layers and trough structures (Figs. 5, 7A). Mafic dikes are rare, and typically disaggregated or associated with enclave swarms (Fig. 8). Pegmatite dikes are observed in addition (see Vugs and Pegmatites section below).

Magma Mingling Zones

Mingling between schlieren and the non-layered granodiorite (KLG) occurs throughout the margin zone. Schlieren are commonly locally re-intruded by

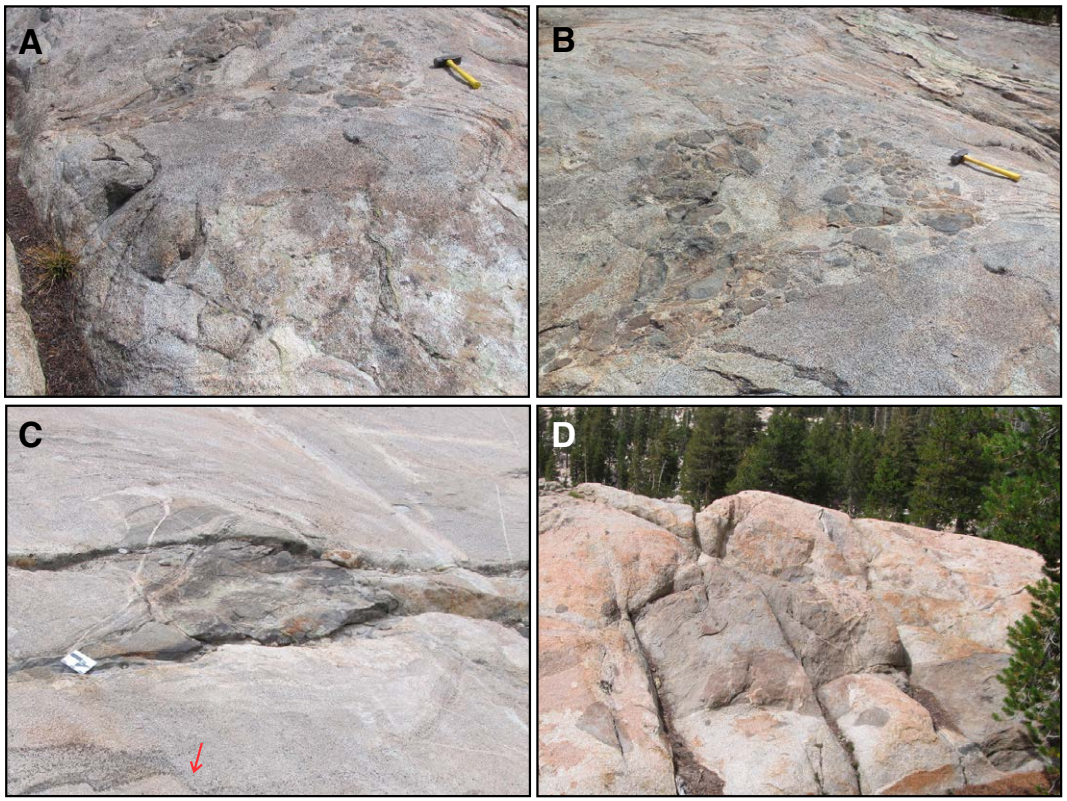

Figure 6. Field photos within the schlieren zone illustrating interactions of schlieren with enclave swarms and stoped blocks. (A) Enclave swarm surrounds block of Kinney Lakes granodiorite (KLG). A meter-scale vug in the upper left of the image records local boiling. Schlieren are observed in the top right of the image. (B) Close-up view of enclave swarm and cognate inclusion shown in A. Enclaves are a wide range of shapes with no clear alignment, include schlieren in the interstitial regions, and are sharply truncated by the cognate inclusion. (C) Layered, stoped block in KLG (likely a cognate inclusion) is cut by leucogranite veins, and normal faults indicated by a red arrow are found in the schlieren layers below the block. Scale bar is 15 cm. (D) Stoped blocks of mafic Bummers Flat granodiorite in the KLG with angular and subrounded edges. Largest block in the photo is ~2 m wide.

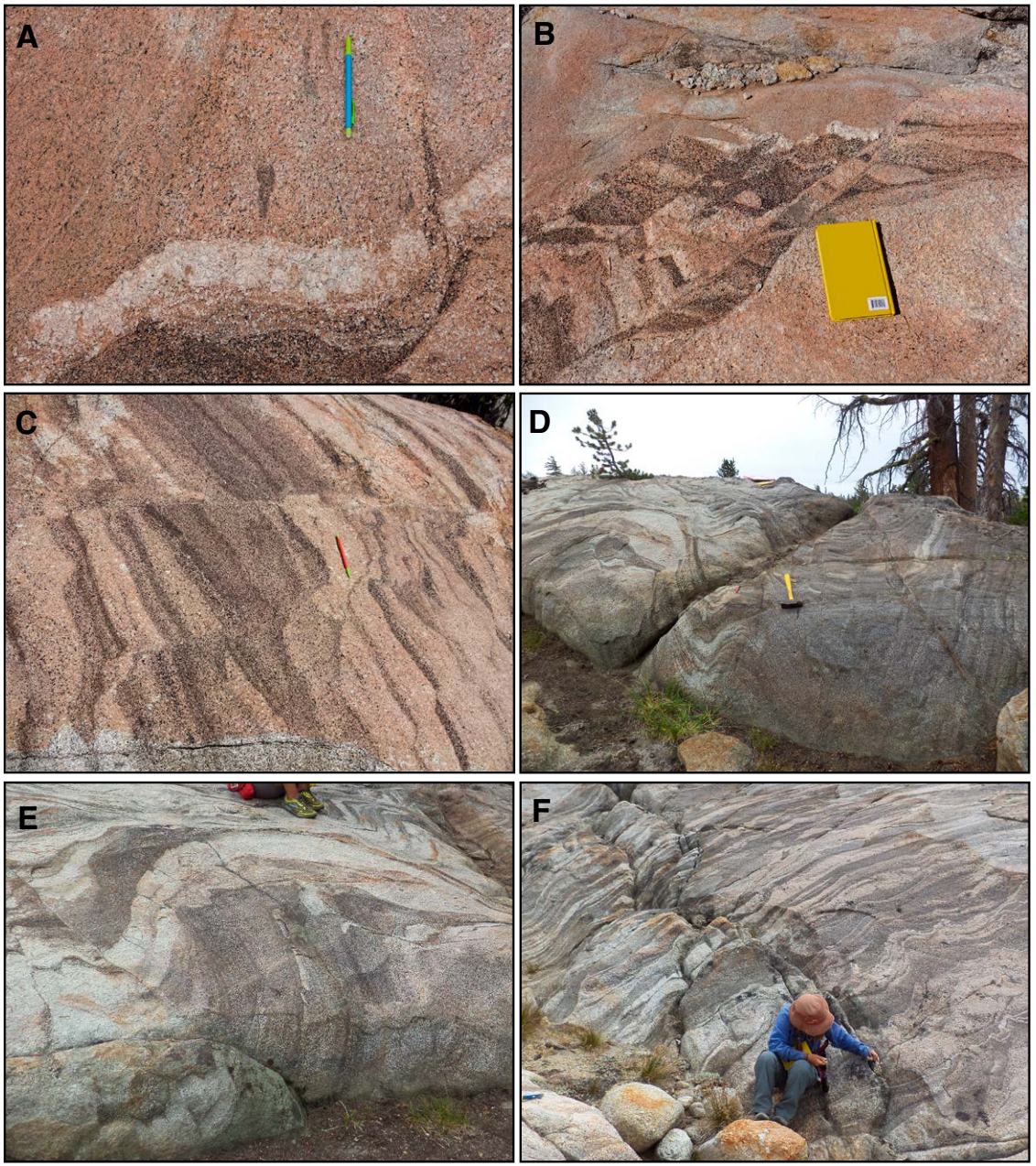

Figure 7. Field photos within the schlieren zone illustrating the different types of deformation-related structures observed. (A) Folded schlieren layer and leucogranite dike, where the regional NW-striking fabric represents the axial planar cleavage (direction of pencil). Enclaves are also aligned with the fabric. (B) Layered schlieren package broken up by faulting. 19 cm notebook for scale. (C) Schlieren package displaced by right-lateral fault running from left to right in the image (above pencil). (D) Outcrop-scale magmatic folds of schlieren layering with a local axial-planar magmatic foliation. Local truncations are visible within the folds, documenting multiple magmatic events. (E) Another view of the outcrop shown in D showing folding and magmatic faulting of schlieren layers. (F) Outcrop-scale view of the schlieren zone with folded and faulted layers.

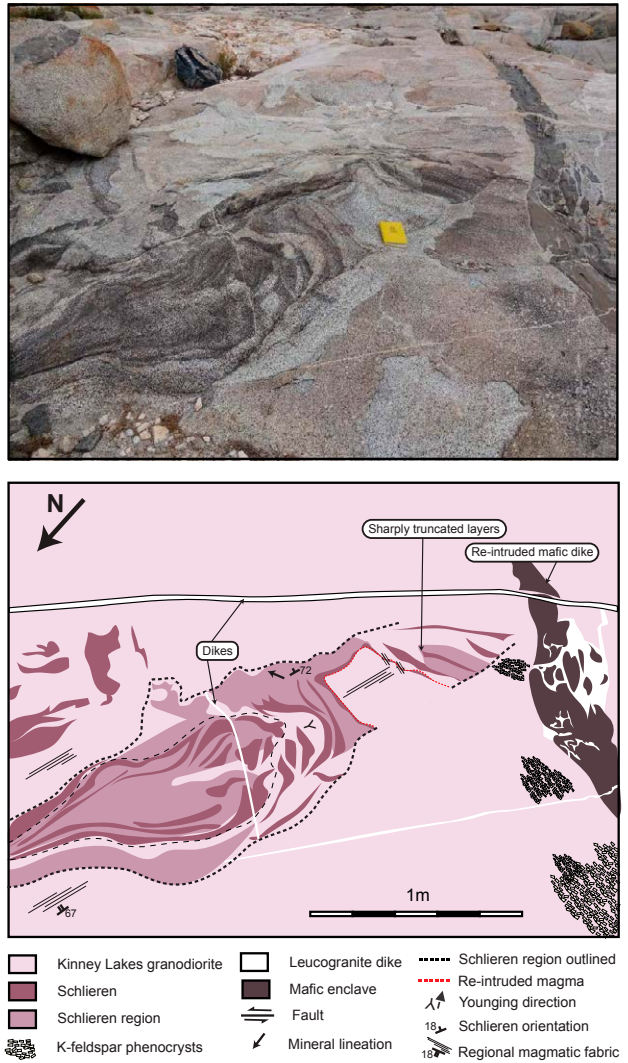

Figure 8. Horizontal outcrop viewed in the southeast direction of deformed schlieren layers in the Kinney Lakes granodiorite (KLG) margin. The regional fabric is well-defined striking north-south (018/67, right-hand rule). Some portions of the KLG in this region have alkali-feldspar clusters, which is atypical for the margins of this unit (the core is more porphyritic). Schlieren dip steeply (357/72) roughly parallel to the regional magmatic mineral foliation. Magmatic mineral lineation is roughly down dip (62/085). Cross-cutting schlieren layers indicate a younging direction toward the north. Schlieren are locally re-intruded by KLG, and nearby, schlieren are folded and faulted magmatically (see red dashed line). The disaggregation of the mafic dike shows magma mingling with the KLG. All structures, including the mafic dike, are cut by late leucogranite veins.

the KLG unit (Fig. 8). The mingling process is commonly associated with some magmatic deformation at the outcrop scale, such as faulting and folding (Figs. 3B, 8). At the scale of a single layer, contacts between schlieren and leucocratic layers are in some places lobate. Locally, features at least superficially similar to load casts are found at the base of schlieren (Fig. 3B). Enclaves also in some cases have lobate boundaries with the host magma.

Xenolith Blocks and Cognate Inclusions

Isolated igneous blocks are ubiquitous near the KLG margin in the mapped area (Figs. 2, 6A–6D). The most common types of blocks are xenoliths of the BFG (sheeted granodiorite, tonalite, and diorite) and cognate inclusions of the KLG. Blocks vary in size from several centimeters to as much as 300 m in length, and the largest blocks found were of BFG xenoliths (Figs. 2, 6C, 6D).

At the map scale, xenoliths are irregular to rectangular in shape with either sharp or subangular corners (Figs. 2, 6C). In outcrop-sized and smaller blocks, margins of BFG xenoliths are commonly sharp and angular, but locally are lobate (Fig. 6D) or, in rare cases, diffuse with the host KLG.

Cognate inclusions of mafic KLG are similar in shape and proportion to BFG xenoliths, but generally with lobate and subrounded edges (Figs. 6A, 6B). They have a similar texture to the KLG in the study area, but differences include a finer grain size, higher content of mafic minerals (a mafic granodiorite), and internal layered structures.

Both types of blocks are commonly associated with leucogranite dikes and veins, where blocks are broken into smaller pieces and/or fractured (Figs. 6C, 6D). Where blocks are associated with schlieren, layer orientations are in some cases arranged parallel to the edges of the largest blocks, with highly variable dips (Fig. 2). The blocks appear to have little to no effect on the orientation of the regional magmatic foliations.

Vugs and Pegmatites

A small number of miarolitic cavities (centimeter scale) and vugs (meter scale) composed of pegmatitic quartz, feldspar, and minor biotite and tourmaline are found in the study area (Fig. 6A). Vugs have spherical to ellipsoidal geometries. Pegmatite dikes are more common, and sometimes are folded (Fig. 7A).

Deformation-Related Structures

Magmatic Faults

Magmatic faults are observed at the KLG margin where they offset planar schlieren and troughs. Faults are mostly normal in the sense of slip, are

oriented at a high angle to the schlieren layering and have minimal displacements <1 m (Figs. 6C, 7B, 7C, 7E, 8). A single magmatic fault may displace multiple schlieren, and within a single outcrop there is evidence for several distinct faulting events (Fig. 5, 7B).

Measurements on fault slip planes indicate an average sense of slip parallel to the contact margin (NNW-SSE trending) with a dip of ~75° and sense of movement down to the east (see stereonet in Fig. 2; $n = 4$). In some cases, magmatic normal faults offset leucogranite dikes that intrude the schlieren zone (Fig. 5). Leucogranite veins are commonly found along the fault plane (Figs. 7B, 7C, 7E). At the fault, the local magmatic fabric in schlieren, defined by hornblende and biotite, was deflected into the fault plane in the magmatic state (Fig. 5). No solid-state deformation is found along faults at the outcrop scale.

Magmatic Folds

Like magmatic faults, magmatic folds at the KLG margin are observed deforming multiple schlieren and trough structures. Magmatic folds vary in wavelength and amplitude over short distances (Figs. 3B, 5, 7A, 7D–7F). Locally, they deform a small number of schlieren layers with thicknesses from top to bottom <2 m. Some schlieren are folded by multiple events (Fig. 5). Folds are distributed throughout the margin zone (Fig. 7F), commonly associated with either magmatic faults (Figs. 5, 7E) or host-rock blocks. In folded schlieren, the orientation of minerals is deflected to a new orientation parallel to the axial plane (Fig. 5). Folds have multiple orientations of axial planes that may be associated with the emplacement of host-rock blocks. A limited number of measured fold axial planes excluding those associated with the host-rock blocks show a weak preference for contact-parallel strikes and a restricted span of dip values (~70°–90°) (see stereonet in Fig. 2; $n = 7$).

SPATIOTEMPORAL RELATIONSHIPS BETWEEN STRUCTURAL ELEMENTS OF THE SCHLIEREN ZONE

The wide variation in magmatic structures preserved at the margin of the KLG allows us to investigate the relative chronology of magmatic events. Below we present evidence pertaining to relative timing relationships between different structures.

The formation of the schlieren, troughs, and enclave swarms were closely intertwined in the study area. Schlieren and enclave swarms are commonly interbedded. Enclave swarms in some cases truncate schlieren packages (Fig. 3C) and vice versa (Fig. 3D). Trough truncations in addition indicate repeated magmatic erosion and redeposition to form new schlieren (Figs. 3B, 4). Schlieren structures (both planar schlieren and troughs) were subsequently re-intruded by KLG (Fig. 8) and deformed by magmatic faults and folds (Figs. 5, 7C–7E). The mingling and re-intrusion of KLG into schlieren (Fig. 8) suggests that the schlieren were in a mush state and could be partly reworked. However, in some cases (e.g., Fig. 8) schlieren behaved as rigid blocks that were displaced and recycled as one cohesive package into the KLG.

The NW-SE and ENE-WSW regional magmatic fabrics defined by hornblende and biotite are locally defined by stretched, aligned enclaves (Fig. 7A). The NW-SE fabric is roughly parallel to the orientation of schlieren, as well as the KLG-BFG contact in the north of the study area. At the map scale, the NW-SE fabric is discordant with the southern contact of the KLG-BFG. Within individual schlieren structures, the local schlieren fabric may be highly discordant with both regional fabrics, and in some cases, the local schlieren fabric is overprinted by the regional fabric(s). In folded schlieren, the regional fabric may be deflected to a new orientation parallel to the axial plane (Figs. 5, 7D).

Stoped blocks of BFG and cognate inclusions of KLG in the study area are typically angular, with a few subrounded shapes, indicating magmatic interaction of the blocks with the KLG. Blocks in some cases truncate enclave swarms (Fig. 6B) and have deformed schlieren at the map and outcrop scale (Figs. 2, 6C), suggesting that they are closely linked in time with both the formation and deformation of the compositionally defined structures. The cognate inclusions of KLG, generally of a more mafic granodiorite composition, also contain a magmatic fabric rotated (as much as 90°) from the strike of the regional magmatic fabrics within the KLG, and were broken and fractured by leucocratic veins and dikes. Indeed, blocks including dike fragments that are in turn surrounded by schlieren indicate that the blocks may have experienced multiple episodes of fracture and movement in the chamber (Fig. 3D).

Field evidence suggests that the leucogranite bodies and dikes were melts draining from the KLG mush (Fig. 5). Dikes are considered in most cases as late features due to their generally high silica compositions and their cross-cutting relationships with stoped blocks (Fig. 6C), schlieren structures (Figs. 3B, 4, 5, 8), and magmatic faults (Fig. 5). Pegmatite dikes and vugs also fit into this category. However, dikes are locally folded and in some cases included as a component of blocks (Figs. 3D, 5), suggesting that they also experienced magmatic deformation and formed at different times during the formation of the KLG margin zone.

Deformation-related structures such as magmatic faults and folds deform multiple, cohesive schlieren packages (Figs. 5, 7B–7E). Thus, they must slightly postdate the formation of the layers. However, Figure 5 shows the complexity in timing relationships, as a package of magmatically folded schlieren is truncated by another package of folded and faulted schlieren. This indicates that deformation was synchronous with the generation of planar schlieren and troughs. In addition, folding and faulting were occurring at the same time (Fig. 5).

PETROGRAPHY AT THE KINNEY LAKES GRANODIORITE MARGIN

Kinney Lakes Granodiorite and Leucogranite

The KLG contains feldspars and quartz together with hornblende, biotite, sphene, magnetite, and accessory apatite and zircon (Table 1). The

grain size of quartz and feldspars (~2–4 mm) in the host unit are considerably larger than in both the schlieren and leucocratic bands. Evidence for intracrystalline deformation is found only in quartz, which displays undulose extinction.

The leucogranite within the KLG unit is composed of plagioclase, quartz, alkali feldspar, and biotite (Table 1). Biotite typically has ragged grain boundaries at some ends (Fig. 9A). In rare cases, it shows undulose extinction where it is pinned against larger feldspar grains. Plagioclase contains magmatic microstructures such as euhedral shapes, concentric compositional zoning, and growth twins (Fig. 9A). Secondary muscovite and sericite are found in some plagioclase crystals. Quartz shows sweeping undulose extinction (Fig. 9A).

Schlieren and Leucocratic Bands

Schlieren bands are dominated by euhedral hornblende, biotite, magnetite, and sphene, with accessory apatite and zircon (Table 1). Plagioclase and quartz occupy the interstitial regions (~0.5–1 mm size), while alkali feldspar is rare. Hornblende, biotite, and sphene are aligned, forming a magmatic fabric in the schlieren, and do not show evidence for lattice distortion. In contrast quartz, occupying interstitial pockets between phenocrysts, shows undulose extinction of both sweeping and chessboard structures (Fig. 9B). Feldspars record intracrystalline deformation in the form of rare deformation twinning, but microstructures are largely magmatic, as growth twinning and zoning are ubiquitous (Fig. 9C). Plagioclase crystal clots are observed, where crystals

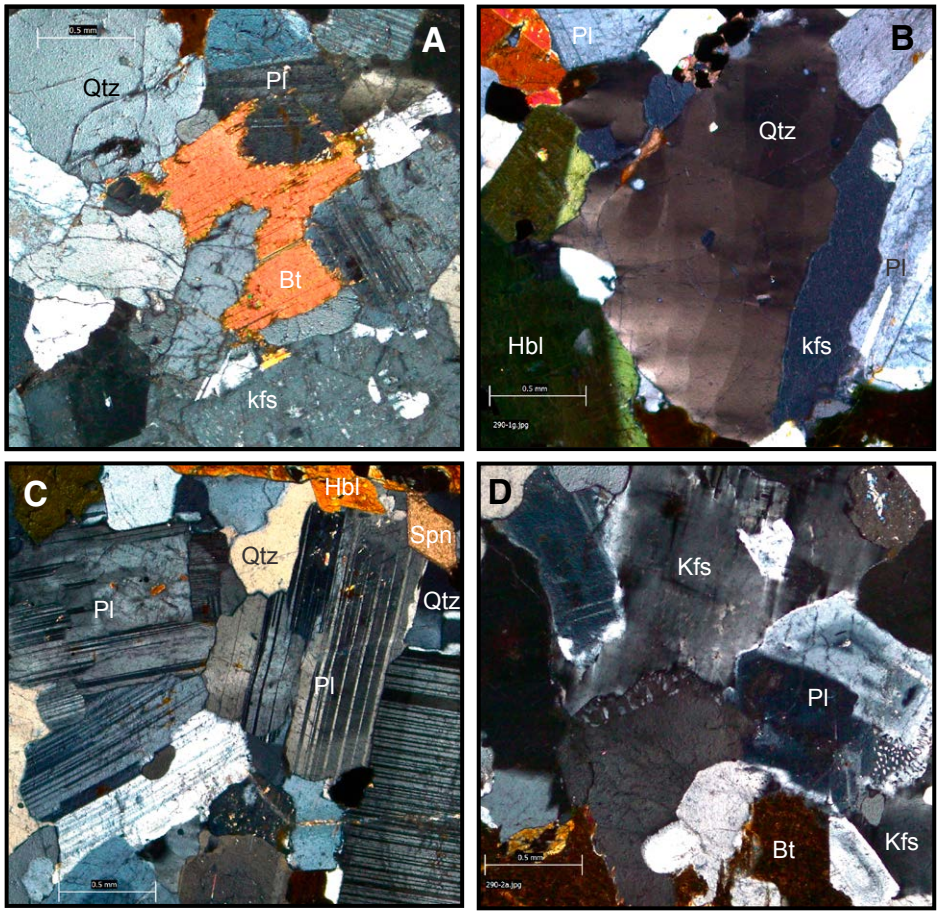

Figure 9. Photomicrographs of leucogranite, schlieren, and felsic layers at the Kinney Lakes granodiorite margin, all under cross-polarized light. Scale bars are 0.5 mm. (A) Sample SWP311 of leucogranite showing the ragged edges of biotite intergrown with plagioclase, alkali feldspar, and quartz, interpreted to be a magmatic growth feature. (B) Sample SWP 290-1 of a schlieren layer showing chessboard undulose extinction in quartz, with unmodified, magmatic margins and dihedral angles. (C) Sample SWP 290-1 of a schlieren layer showing a clot of plagioclase crystals. Note that the plagioclase twins are largely growth twins, with a few exceptions that are deformation twins. Plagioclase-plagioclase boundaries are low angle or parallel to growth twins, with few boundaries at high angle to growth twinning. (D) Sample SWP 290-2 felsic band in schlieren showing graphic microstructure between plagioclase and alkali feldspar, and between alkali feldspar and quartz. This microstructure appears to form preferentially within pools and along grain boundaries. Pl—plagioclase; Qtz—quartz; Hbl—hornblende; Bt—biotite; Kfs—K-feldspar; Spn—sphene.

truncate growth zoning, indicative of synneusis or mechanical clumping. Qualitative observations of grain boundaries and dihedral angles are comparable to those described by Holness et al. (2018) for plutonic units dominated by magmatic crystallization (Fig. 9C). Rare quartz subgrains, fractured amphibole, and glide twins in plagioclase are suggestive of some late crystal deformation during settling and compaction in the presence of melt.

Leucocratic bands between schlieren are dominated by plagioclase and alkali feldspar, with lesser amounts of euhedral hornblende, biotite, and magnetite (Table 1). Leucocratic bands display all of the microstructures contained within schlieren, but at a lower intensity. For example, undulose extinction in quartz is not as pervasive as in the schlieren. Graphic texture is common in the leucocratic bands (Fig. 9D). In these samples, it forms from the intergrowth between plagioclase and alkali feldspar and between quartz and alkali feldspar, occurring at and along grain boundaries and as pools between grains.

WHOLE-ROCK GEOCHEMISTRY

Southwestern Host Rock of the Sonora Pass Intrusive Suite

Two samples of the Bummers Flat granodiorite (BFG) host rock show contents of SiO_2 ~67%, TiO_2 ~0.4%, FeO^{total} of 3% and 4.8%, CaO ~3%, and alkalis ~6% with a Na_2O/K_2O ratio ≥1 (Table 2). In the alkalis versus silica classification diagram, the compositions plot in the granodiorite field (Fig. 10A). The samples have ASI (aluminum saturation index) values of ~1.06 (i.e., slightly peraluminous), and they plot in the medium- to high-K fields on a K_2O versus SiO_2 diagram (Fig. 10B). They show contents of Rb ≤ 115 ppm, Ba ≤1462 ppm, Sr ≤406 ppm, Nb ≤9.5 ppm, Y ≤17.8 ppm, Yb = 1.7 ppm (one value), and Zr ≤153 ppm (Table 2). The chondrite-normalized (N) REE pattern of one sample shows La_N/Yb_N ratio of ~11 and a moderate Eu anomaly (Eu_N/Eu_N^* = 0.7) (not shown).

Compared to the BFG, mafic intrusions show lower SiO_2 contents (≤48%) with relatively high TiO_2 (≤1.7%), FeO^t (≤13.7%), CaO (~9%), and alkalis (~4%) with variable values of the Na_2O/K_2O ratio (Table 2). These two mafic samples in the alkalis versus silica classification diagram plot in the gabbro and foid gabbro fields (Fig. 10A). In a K_2O versus SiO_2 diagram, the gabbro falls in the medium-K field whereas the foid gabbro plots in the high-K field (Fig. 10B). ASI values are ~0.7, i.e., metaluminous. They show relatively low contents of Rb ≤108 ppm, Ba ≤275 ppm, Nb ≤3.6 ppm, Y ≤17.1 ppm, Yb ≤1.3 ppm, and Zr ≤72 ppm, and high Sr contents of ≤754 ppm (Table 2). REE patterns of the two gabbroic samples are flat (La_N/Yb_N ratios ~5) with either no Eu anomaly or a positive one (Eu_N/Eu_N^* = 1 and 1.12) (not shown).

Sonora Pass Intrusive Suite

The older plutonic unit, the Kinney Lakes granodiorite (KLG), does not show a large variation in major elements. It has restricted contents of SiO_2 (61%–68%), TiO_2 (0.4%–0.8%), FeO (3.3%–6.2%), CaO (3.3%–5.5%), and alkalis (5.7%–6.8%), with a Na_2O/K_2O ratio usually >1 (Table 2). Most of the samples fall in the granodiorite field in the alkalis versus silica classification diagram, and in the high-K field on a K_2O versus SiO_2 diagram (Figs. 10A, 10B). ASI values range from 0.97 to 1.01 (average 0.98, n = 10), i.e., metaluminous to slightly peraluminous. In line with major elements, contents of Rb (85–131 ppm), Ba (649–1141 ppm), and Sr (426–641 ppm) have restricted ranges. In contrast, a wider range in values of Nb (2.2–10.8 ppm), Y (6.7–11.2 ppm), Yb (0.5–1.3 ppm), and Zr (99–150 ppm) is observed (Table 2). The variation in the heavy REE contents is reflected in the variable REE patterns with a wide range of values of the La_N/Yb_N ratio from 10 to 24 (Fig. 10C). There are small negative Eu anomalies in the studied samples (Eu_N/Eu_N^* = 0.79–0.97).

The leucogranite sample has contents of SiO_2 = 73%, TiO_2 = 0.1%, FeO^t = 1.2%, CaO = 1.7%, and alkalis = 7.7% (Na_2O/K_2O ratio ≤1) (Table 2). It is classified as granite in the alkalis versus silica classification diagram, and in the high-K field on a K_2O versus SiO_2 diagram with tendency toward the leucogranite field (Figs. 10A, 10B). ASI value is equal to 1.13, i.e., peraluminous. The leucogranite has contents of Rb = 127 ppm, Ba = 415 ppm, Sr = 249 ppm, Nb < 0.2 ppm, Y = 3.1 ppm, Yb = 0.4 ppm, and Zr = 54 ppm (Table 2). It exhibits a steeply dipping REE pattern (La_N/Yb_N = 28) with a positive Eu anomaly (Eu_N/Eu_N^* = 1.26) (Fig. 10C).

The Topaz Lake granodiorite, the youngest unit in the suite, also shows a restricted range in major elements, although in comparison to the KLG it tends toward more felsic end members. It shows ranges in SiO_2 contents between 67%–71%, TiO_2 = 0.2%–0.5%, FeO = 2%–3.6%, CaO = 0.9%–3.6%, and alkalis = 6.5%–8.3% (Table 2). The Na_2O/K_2O ratio is usually >1. The samples plot in the granodiorite and granite fields in the alkalis versus silica classification diagram, and in the medium- to high-K fields on a K_2O versus SiO_2 diagram (Figs. 10A, 10B). ASI values range from 0.99 to 1.05 (average 1.01, n = 13), i.e., metaluminous to slightly peraluminous. The granitic samples have contents of Rb = 101–166 ppm, Ba = 125–1227 ppm, Sr = 408–615 ppm, Nb = 6.9–9.7 ppm, Y = 8.5 ppm (two values), Yb = 0.5–0.7 ppm, and Zr = 99–133 ppm (Table 2). The REE patterns show La_N/Yb_N ratios between 22 and 29 and weak to moderate Eu anomalies (Eu_N/Eu_N^* = 0.8–0.9) (not shown).

Schlieren Zone in the Kinney Lakes Granodiorite

Schlieren in the KLG have relatively low SiO_2 contents (54%–61%) but high TiO_2 (1.2%–1.8%), FeO (8.1%–12.7%), CaO (3.9%–6.2%), and alkalis (5.7%–6.6%) (Table 2). The Na_2O/K_2O ratio is usually <1. Samples plot between the monzodiorite and tonalite fields in the alkalis versus silica classification diagram, and in the high-K field on a K_2O versus SiO_2 diagram (Figs. 10A, 10B). ASI values range from 0.80 to 0.86 (average 0.82, n = 3), i.e., metaluminous. They have contents of: Rb = 102–154 ppm, Ba = 438–621 ppm, Sr = 212–368 ppm, Nb = 16–26 ppm, Y = 28–46 ppm, Yb = 2.5–4 ppm, and Zr = 268–405 ppm (Table 2). REE patterns show La_N/Yb_N ratios from 10 to 19 and moderate Eu anomalies (Eu_N/Eu_N^* = 0.66–0.73) (Fig. 10C).

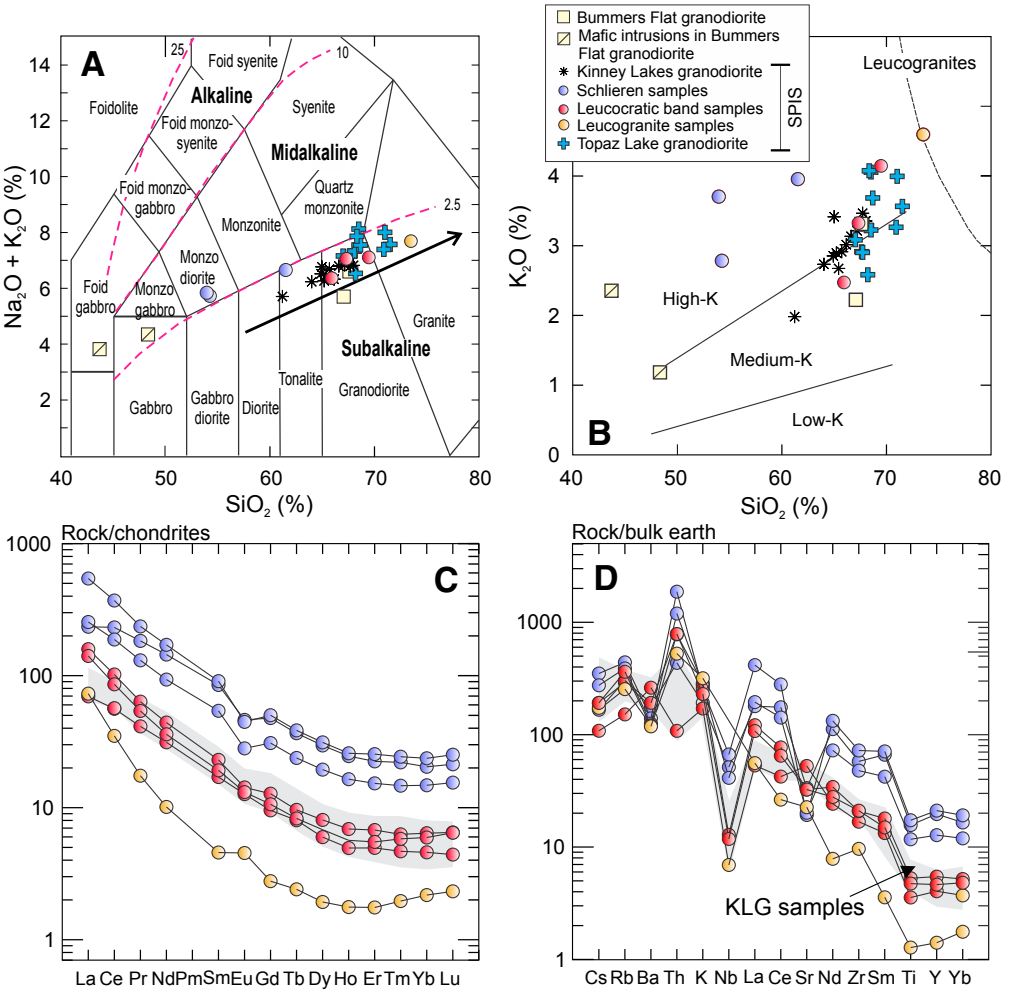

Figure 10. (A, B) Total alkali versus silica diagram after Middlemost (1994) (A) and K_2O versus SiO_2 diagram with classification boundaries after Le Maitre (1989) (B) for the studied samples. The alkaline, mid-alkaline, and subalkaline magmatic lineages in (A) are defined by sigma isopleths (after Rittmann, 1957). (C) Chondrite-normalized (after Sun and McDonough, 1989) rare earth element plot for the samples of igneous layering and the host Kinney Lakes granodiorite (KLG). (D) Bulk earth-normalized (after Hickey et al., 1986) values plot for the samples of igneous layering and the host KLG. SPIS—Sonora Pass Intrusive Suite.

Leucocratic bands have high SiO_2 contents (66%–69%) but low TiO_2 (0.37%–0.55%), FeO (3.2%–3.8%), CaO (2.9%–4.5%), and alkalis (6.4%–7.1%) (Table 2) with variable values of the Na_2O/K_2O ratio. The samples plot in the granodiorite field in the alkalis versus silica classification diagram, and they plot in the medium- to high-K fields on a K_2O versus SiO_2 diagram (Figs. 10A, 10B). ASI values range from 0.96 to 1.03 (average 0.99, $n = 3$), i.e., metaluminous to slightly peraluminous. They have relatively high contents of Ba (423–916 ppm) and Sr (357–579 ppm) but lower Rb (53–106 ppm), Nb (2.7–5 ppm), Y (8.9–12 ppm), Yb (0.8–1.1 ppm), and Zr (94–118 ppm) (Table 2). REE patterns show La_N/Yb_N ratios from 12 to 21 and weak or no Eu anomalies ($Eu_N/Eu_N^* = 0.83–0.99$) (Fig. 10C).

Rb-Sr AND Sm-Nd WHOLE-ROCK ISOTOPE COMPOSITIONS

A reference age of 95 Ma is used for calculating isotope compositions at the time (t) of magma crystallization in the KLG, from the weighted U-Pb sensitive high-resolution ion microprobe (SHRIMP) zircon age of one granodiorite sample (Leopold, 2016). Compared with the published data of eight samples of the KLG ($0.7056 \leq {}^{87}Sr/{}^{86}Sr_{(t)} \leq 0.7058$) (Macias, 1996), our samples (SWP-311 and SWP-312) of the KLG yield similar ${}^{87}Sr/{}^{86}Sr_{(t)}$ values of 0.7060 and 0.7057 (Table 3). The leucogranite and granodiorite samples have $\varepsilon_{Nd(t)}$ values of –2.8 and –2.6 respectively (Table 3).

Two samples (SWP-290-1 and SWP-307-1) of schlieren have $^{87}Sr/^{86}Sr_{(t)}$ values of 0.7056 and 0.7057, and $\varepsilon_{Nd(t)}$ –3.1 (Table 3). The leucocratic counterparts of these layers (samples SWP-290-2 and SWP-307-2) yield $^{87}Sr/^{86}Sr_{(t)}$ and $\varepsilon_{Nd(t)}$ values of 0.7058 and ~–3, respectively (Table 3).

The analyzed samples are depleted in Rb, with whole-rock contents between 89 and 154 ppm (Table 2). One granodiorite sample (SWP-312) and two leucocratic bands (SWP-290-2 and SWP-307-2) have high Sr contents (357–496 ppm), but the two schlieren and leucogranite have <250 ppm, resulting in a wide range of Rb/Sr ratios. Including the KLG leucogranite (sample SWP-311), the six samples fall on an errorchron corresponding to an age of 94 ± 19 Ma (mean square of weighted deviates or MSWD = 13). However, if the leucogranite sample is not considered, an isochron (MSWD = 2.6) is defined with an age of 91.9 ± 9.6 Ma and an initial $^{87}Sr/^{86}Sr$ ratio of 0.70581 ± 0.00018 (Figs. 11A, 11B).

DISCUSSION

Origin of the Schlieren in the Kinney Lakes Granodiorite

Petrographic observations indicate that both schlieren and leucocratic bands contain the same mineral assemblage as the host granodiorite but have different modal abundances (Table 1; see also Reid et al., 1993; Solgadi and Sawyer, 2008; Paterson, 2009). This is consistent with Sr and Nd whole-rock isotope compositions, where the studied layered samples and the host granodiorite show restricted ranges of $^{87}Sr/^{86}Sr_{(t)}$ = 0.7056–0.7060 and $\varepsilon_{Nd(t)}$ = –2.6 to –3.1, regardless of the wide range in SiO_2 content (54%–74%) (Fig. 11C; Tables 2, 3). They plot in the $^{87}Sr/^{86}Sr_{(t)}$ versus $\varepsilon_{Nd(t)}$ diagram without any dispersion, indicating that all samples crystallized from the same magma (Fig. 11D). In the same way, the acceptable isochron of five samples with an age of 91.9 ± 9.6 Ma and

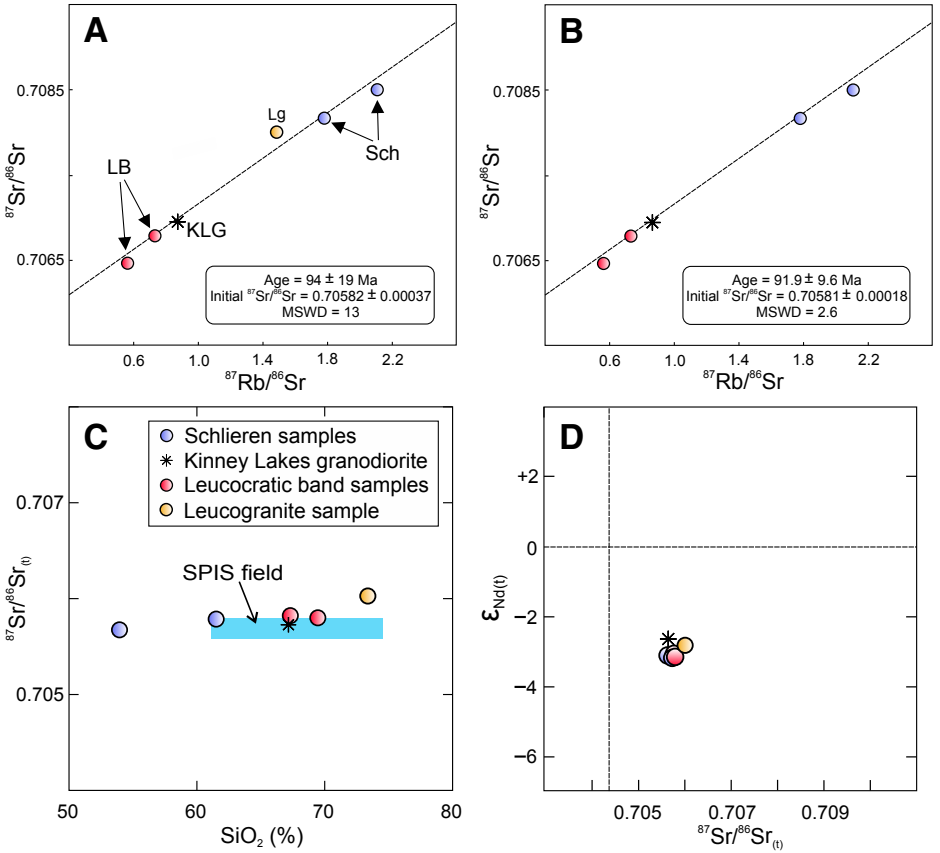

Figure 11. (A) Rb-Sr errorchron plot which includes two schlieren samples (Sch), two leucocratic band samples (LB), a leucogranite (Lg), and one sample of the Kinney Lakes granodiorite (KLG). (B) Rb-Sr isochron plot excluding sample SWP311, a leucogranite (Lg in panel A). The data are given in Table 3. MSWD—mean square of weighted deviates. (C, D) SiO_2 versus $^{87}Sr/^{86}Sr$ initial (C) and $^{87}Sr/^{86}Sr$ initial versus $\varepsilon_{Nd(t)}$ plots (D) for the studied granitic rocks. In C, the Sonora Pass Intrusive Suite (SPIS) field is formed by one sample of this work and 20 samples (nine samples of KLG and 11 samples of Topaz Lake granodiorite) from Macias (1996).

an initial $^{87}Sr/^{86}Sr = 0.70581$ is consistent with a co-magmatic origin (Fig. 11B), and further suggests that the Rb-Sr age records whole-rock system closure immediately after crystallization of the pluton at 95.6 ± 1.5 Ma (Leopold, 2016). The KLG leucogranite sample (SWP-311) excluded in the isochron, with a high abundance of secondary muscovite, probably reflects some perturbation of the Rb-Sr systematics after crystallization by a local fluid event.

Chemically, the schlieren, leucocratic band samples, leucogranite, and host granodiorite of Kinney Lakes define a clear trend on major-element diagrams (trend 1 in Fig. 12). The SiO_2 versus $FeO^t + MgO + TiO_2$ and the $TiO_2 + FeO^t +$ K_2O versus P_2O_5 plots show trends with correlation coefficients (r) close to 0.9 for all samples (Figs. 12A, 12B). Trend 1 is consistent with crystal fractionation, in which dense mafic crystals represented in the schlieren are separated from KLG magma resulting in a feldspar- and silica-rich melt (leucocratic bands and leucogranite). A similar trend (trend 2 in Fig. 12) is shown in the same diagrams for the granitic samples of the SPIS (excluding the layered structures and the leucogranite), where the Topaz Lake granodiorite samples have a more differentiated composition than KLG samples. However, on the FeO^t versus CaO plot, only the SPIS granitic samples form a clear trend (trend 2)

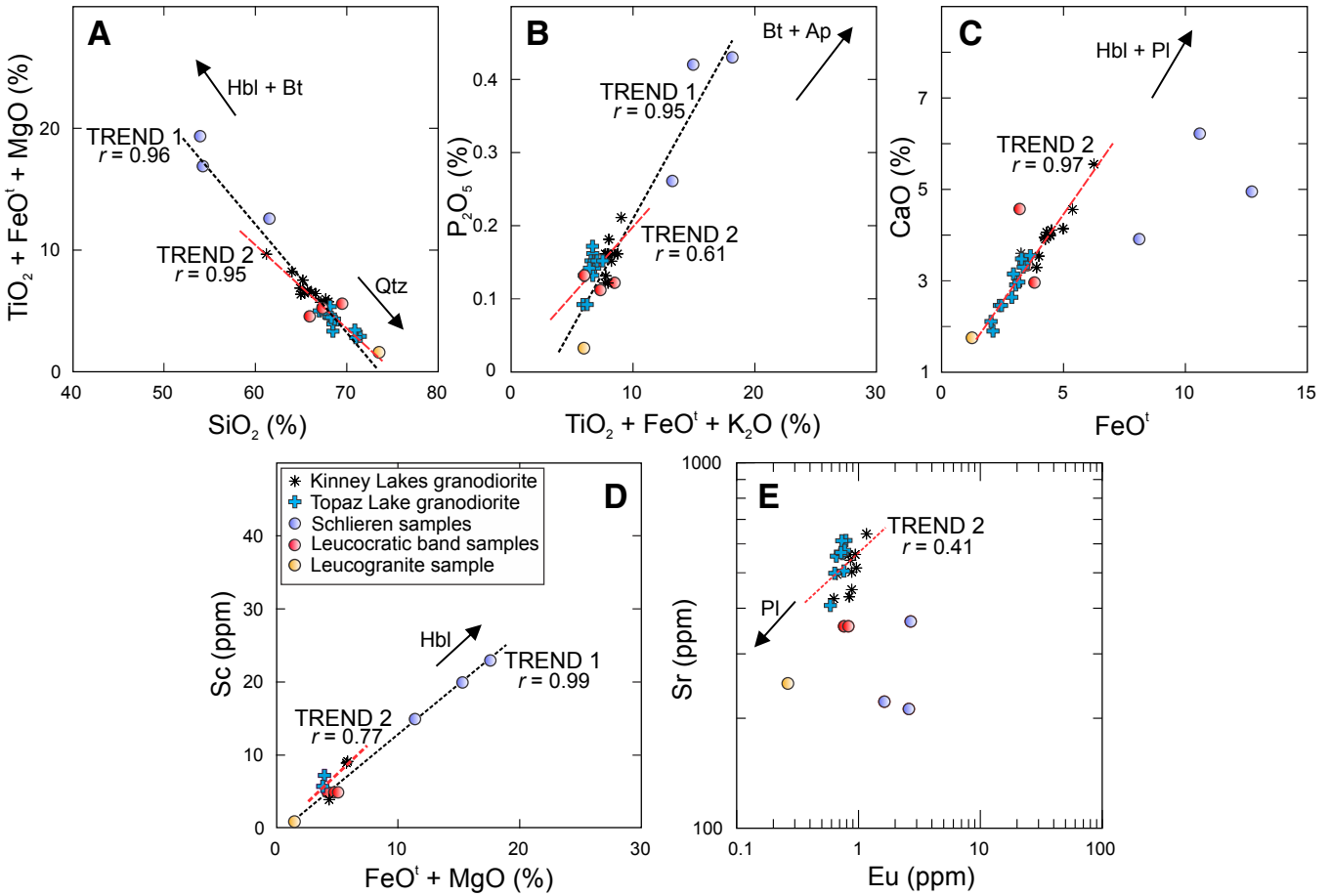

Figure 12. Plots for the Sonora Pass Intrusive Suite and igneous layering samples. (A) SiO_2 versus $TiO_2 + FeO^{total} + MgO$. (B) $TiO_2 + FeO^t + K_2O$ versus P_2O_5. (C) FeO^t versus CaO. (D) $FeO^t + MgO$ versus Sc. (E) Eu versus Sr. Note log scale in E. Arrows reflect crystallization of different minerals based on the whole-rock geochemistry; the sense of the arrow indicates a greater modal mineral proportion. Trend 1 is defined by schlieren, leucocratic band samples, leucogranite, and samples of Kinney Lakes granodiorite. Trend 2 is formed by granitic samples of the Sonora Pass Intrusive Suite, excluding the layered structures and the leucogranite. Hbl—hornblende; Bt—biotite; Qtz—quartz; Ap—apatite; Pl—plagioclase.

(Fig. 12C). Schlieren samples move away from the differentiation trend 2, which is dominated by fractionation of hornblende + plagioclase, toward values higher in FeO^t by almost exclusive fractionation of mafic minerals and subordinate plagioclase.

Trace-element abundances in the layered structures are also in concordance with a selective separation of mafic minerals from the KLG magma. The high modal proportion of biotite, hornblende, and accessory minerals (including zircon, sphene, apatite, and opaque minerals) in the schlieren is reflected in the enrichment of REEs, Y, and Zr relative to the leucocratic band samples and the leucogranite (Fig. 10D). Moreover, the acceptable correlation between FeO^t + MgO against Sc, which is highly fractionated by hornblende, describes a good correlation (r = 0.99) for trend 1 (Fig. 12D). In contrast, samples of trend 1 show no correlation in the logarithmic plot of Eu versus Sr concentrations (Fig. 12E). The Sr decrease with decreasing Eu showing the role of feldspar fractionation is only evident in SPIS samples (trend 2). Therefore, during schlieren formation, feldspar fractionation was decoupled in relation to that of the mafic minerals. We envisage that this fractionation at the solidification front could have been aided by external factors, such as strain rate and imposed stress, to expel lighter minerals and/or felsic liquid from the schlieren.

REE patterns of both layered and non-layered rocks are mostly parallel (Fig. 10C) but with differences in both their abundances and in the magnitude of the Eu anomaly. This behavior, also reported in other layered structures in the Sierra Nevada (e.g., Reid et al., 1993; Solgadi and Sawyer, 2008), implies that the schlieren-forming process did not discriminate between the different types of REE-bearing minerals hosted in the KLG magma. These different minerals, mostly accessory phases, were distributed almost homogeneously in the study area but concentrated in variable proportions between schlieren and KLG, which supports the idea that schlieren formed from the KLG. This is also supported by the parallel REE patterns of the schlieren samples to those of the host KLG. Schlieren show a higher abundance of most of the elements and a moderate negative anomaly of Eu (Eu_N/Eu_N^* = 0.66–0.73) due to a lower plagioclase content. The total REE content in the schlieren (260–505 ppm) far exceeds the range of values of the KLG (76–130 ppm). In contrast, the lower modal content of the mafic minerals and high modal content of feldspar in the leucogranite sample show a depletion in heavy REEs, with a total content of 48 ppm and a positive Eu anomaly (Eu_N/Eu_N^* = 1.28). The leucocratic bands show both identical REE patterns and a similar content of total REEs (78–138 ppm) to those of KLG, except for a weak or absent Eu anomaly (Eu_N/Eu_N^* = 0.84–0.99), indicating a higher fraction of plagioclase.

From a mass-balance perspective, a simple two-component linear mixing calculation (e.g., Fourcade and Allegre, 1981) on major elements suggests that the mixing between the leucocratic band and schlieren (model A in Table 4) can reproduce the bulk composition of the KLG with a very acceptable regression line (r^2 = 0.99). However, this mixture of 14% schlieren and 86% leucocratic band is unrealistic in a closed-system model (where there is no melt migration outside of the schlieren zone) because proportions of the schlieren and leucocratic bands in the field are close to 1:1 (Figs. 3A, 7F). Such a model requires that a significant proportion of magma, compositionally similar to the leucocratic bands, is expelled toward the chamber interior, or to shallower levels of the plumbing system. Using the leucogranite sample as the differentiated end member (model B in Table 4) provides a similar value of the regression line (r^2 = 0.95) to model A but with a bulk mixture of ~42% schlieren and 58% leucogranite. This implies that leucogranite dikes may reflect the fractionated melts removed from schlieren, rather than the felsic layers found in between the schlieren.

Therefore, we speculate that the magmatic system was an open system, where leucogranitic melts may have been extracted from the schlieren zone. The melt could either have escaped the system to the chamber interior or to shallower levels, readily diffused, and mixed back in with melts of the KLG, or locally pooled and formed dikes and leucogranite bodies. This can explain why the chemical signature of the differentiated end member from schlieren is difficult to trace.

In summary, whole-rock chemical data support the hypothesis that the main mechanism of schlieren formation was fractional crystallization in an isotopically closed system, mainly by effective segregation of mafic minerals plus accessory phases with drainage and migration of leucogranitic melts back into the KLG or to shallower levels. The decoupling of plagioclase ± quartz in the schlieren chemistry illustrates that liquid-crystal fractionation was selective and did not depend solely on gravitational forces, but that other factors, such as deformation-assisted reorganization of the crystal mush, were required to promote leucogranitic melt migration away from the schlieren zone (see next).

TABLE 4. TWO-COMPONENT MIXTURE CALCULATION

$C^i_M = xC^i_A + (1 - x)C^i_B$
$C^i_M = xC^i_A + C^i_B - xC^i_B$
$C^i_M - C^i_B = x(C^i_A - C^i_B)$

Model A

C^i_A—average of leucocratic band samples (SWP278-3, SWP290-2, and SWP307-2)
C^i_B—average of schlieren samples (SWP278-2, SWP290-1, and SWP307-1)
C^i_M—average of Kinney Lakes granodiorite (KLG) samples (SICN17, SICN25, SWP312, S10-2, S72-3, S72-4, S52-2, S22-8, R52-9, and S28-8)
R^2 = 0.99 C^i_A in the mixing = 86%

Model B

C^i_A—leucogranite sample (SWP-311)
C^i_B—average of schlieren samples (SWP278-2, SWP290-1, and SWP307-1)
C^i_M—average of KLG samples (SICN17, SICN25, SWP312, S10-2, S72-3, S72-4, S52-2, S22-8, R52-9, and S28-8)
R^2 = 0.95 C^i_A in the mixing = 58%

Notes: Two-component mixture calculation based on Fourcade and Allegre (1981) C^i_M—content of i element in the mixture formed by two components; C^i_A—content of i element in felsic member; C^i_B—content of i element in mafic member; x—weight proportion of felsic to mafic member in the mixture for each element (i).

Spatiotemporal and Structural Relationships in the Schlieren Zone

Field and Structural Data

The orientation of the schlieren zone parallel to the orientation of the KLG margin indicates that it was controlled by the geometry of the magma chamber. The growth and younging direction of the schlieren zone, determined by mineral gradation of the layers and cross-cutting relationships, was toward the interior of the chamber, where regional magmatic fabrics developed coincidentally with the formation and deformation of schlieren (Figs. 2, 4, 6; Spatiotemporal Relationships between Structural Elements of the Schlieren Zone section).

The intrusive contact between the BFG and the KLG is highly discordant and steep, which, together with the existence of numerous BFG host-rock blocks and KLG cognate inclusions in the schlieren zone, supports the interpretation that the host rock was removed and earlier parts of the KLG margin were recycled during the formation of the schlieren (e.g., Irvine et al., 1998). This is most noticeable in the southern part of the intrusive contact. In this area, the greater variability in the dip of schlieren (Fig. 2) may be explained by the sinking of blocks during schlieren formation. At the same time, enclave swarms commonly truncate schlieren packages, and are themselves truncated by overlying schlieren packages, implying episodic, or cyclic, erosional and magma mingling processes during schlieren formation, all of which likely occurred in situ (e.g., Paterson et al., 2016).

The associated magmatic faults and folds within schlieren packages suggest that the crystal mush was deformed magmatically in a highly dynamic environment. Faults affecting both planar and multiply folded schlieren packages attest to several distinct deformation events during both formation and collapse of the crystal mush (Paterson, 2009; Humphreys and Holness, 2010). Folds have variable axial-planar orientations, reflecting the heterogeneity of folding and deformation at the outcrop scale during magma avalanching. Magmatically folded schlieren are commonly truncated by younger packages of folded and faulted schlieren recording multiple phases of deformation at a single outcrop.

Petrographic and Microstructural Data

Schlieren, leucocratic bands, and the KLG unit show predominantly magmatic microstructures (Fig. 9). Some quartz grains show evidence of intracrystalline deformation in all samples, which could be attributed to stresses during cooling of late-stage melts. A small number of feldspars show deformation twinning. However, the overall amount of deformation is minimal and localized, and there is only slight variation between the type and intensity of the microstructures contained within schlieren and the host granodiorite. This suggests that the overall crystal framework is magmatic with sub-magmatic to solid-state microstructures developed locally due to crystal-crystal stresses and not a throughgoing tectonic strain. Both truncation of compositional zoning in feldspar and interstitial quartz-feldspar in the schlieren are consistent with mineral compaction and melt removal processes in the crystal mush (Fig. 9C).

A Model for the Generation of the Schlieren Zone in the Kinney Lakes Granodiorite

Our model for the formation of the schlieren zone involves the construction of an incipient solidification front on an upper margin of the chamber (Fig. 13). This front, primarily controlled by the geometry of the magma-chamber margin, experiences a larger heat loss than the interior, resulting in an increase in the crystallinity, density, and viscosity of the magma (Marsh, 1996). These denser, crystal-rich magmas become unstable against the boundary with the more-interior, less-viscous magmas and occasionally collapse, leading to downward transport and avalanching of dense crystal slurries by gravity-assisted flow

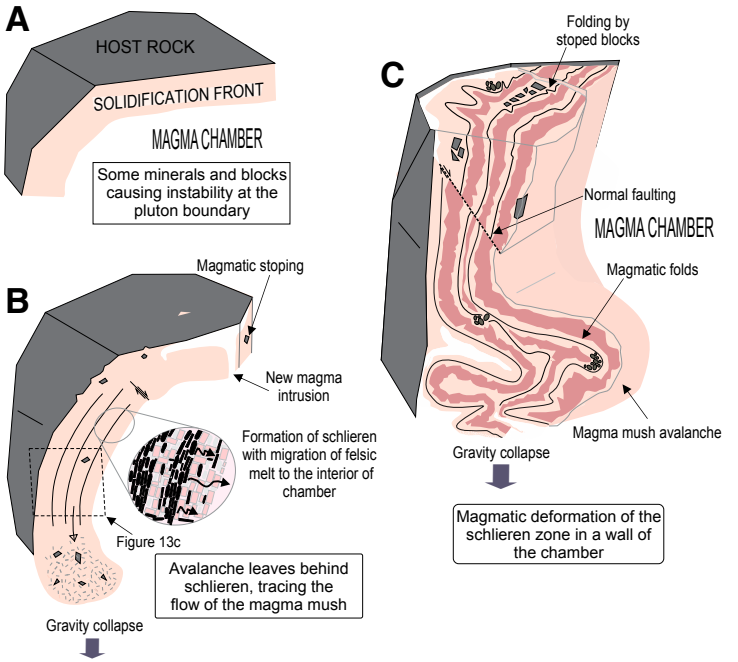

Figure 13. Interpretive block diagrams illustrating the magmatic evolution at the margin of the Kinney Lakes granodiorite (KLG). (A) Formation of an early solidification front in the KLG. (B) Initiation of gravitational collapse of the solidification front and formation of layering by laminar flow. Instability causes crystals to avalanche along the pluton boundary, and incorporates pieces of host rocks and cognate inclusions. (C) Advanced stage of magma avalanching with syn-magmatic deformation structures (fault and fold) related to the transport and reorganization of the crystal-rich pile on a wall of the chamber. The propagation of normal magmatic faults shows directions of slip parallel to the contact margin.

(Irvine et al., 1998; Solgadi and Sawyer, 2008; Žák and Paterson, 2010; Paterson et al., 2016, 2019). Based on field relationships, schlieren formation was discontinuous and repeated in time. Magmatic erosion and redeposition of schlieren was pervasive, and commonly the schlieren packages record evidence of early and later repeated deformation events during magma avalanching.

Field evidence suggests that other mechanisms such as stoping and the presence of a fluid phase could also have triggered a large-scale destabilization of the solidification front. Blocks of host rocks falling into the crystal mush may have created instability by increasing the weight of the mush and exceeding the yield stress of the magma. The presence of a late, exsolved fluid phase, recorded by miarolitic cavities, vugs, and pegmatites, could have generated progressive fluidization by excess pressure in the hydrogranular medium, which is generally governed by multi-phase interactions of silicate liquid, crystals, and bubbles (e.g., Sumita and Manga, 2008; Petford, 2009; Bergantz et al., 2017). In this context, the downward collapse of the crystal-rich margin transported crystals and surrounding magma along the pluton margin, generating the most commonly observed schlieren with a normal density grading and inverse size gradation toward the top of the layer. Their formation was accompanied by strain, compaction, and filter pressing. As a result, both the dense crystals (biotite, hornblende, sphene, and opaque minerals) and in some cases small mafic enclaves are sorted against steeply dipping walls. However, the chemistry suggests that the simple model of physical, mechanical separation of suspended minerals from the magma, combined with crystal settling and compaction, does not fully explain the composition or structural features of the schlieren, and that additional processes are required. During magma mush avalanching, local convection and late hypersolidus strain may have promoted density-driven mineral sorting against steeply dipping walls, forming a transient crystal framework (e.g., Irvine, 1987; Hodson, 1998, Blanchette et al., 2004). This framework was connected to felsic intergranular melt, which may have been displaced toward the interior of the magma body, outside in the BFG host rock or to higher (unexposed) levels. The felsic intergranular melt could have partially contributed to the formation of the leucocratic bands, or remixed with the host magma. We envision that both gravity and local convection driven by internal thermal, compositional, and rheological gradients (Martin et al. 1987) acted on the hydrogranular slurry and mechanically separated the silica-rich melt from the dense crystals.

Kinematic indicators in the schlieren zone are consistent with syn-magmatic deformation and displacement of magma downwards. The propagation of normal magmatic faults with directions of slip parallel to the contact margin resembles slope instability, where material moves downslope in response to gravity (Figs. 2, 5). We find that magmatic faulting and folding record local deformation of the crystal mush after magma avalanching eroded and deposited schlieren. Faults and folds are evidence supporting slumping and settling of the crystal-rich pile. Additionally, magmatic folding and faulting could have been triggered by tectonic or internal magma-chamber processes at a larger scale. For example, the folds with NNW-SSE–trending axial planes with steep dip (~80°) and contact-parallel strike (see above) are also consistent with the shortening direction of regional tectonic forces. Magma-chamber processes could have included the intrusion of new magma batches, or overpressure- or convection-related forces in the interior parts of the magma body directed toward chamber margins. However, to test this hypothesis further, it will be necessary to obtain a greater number of structural measurements of folds.

Possible Causes of Magma Avalanches in Chambers

The formation of a schlieren zone by the growth and collapse of a solidification front requires not only enough melt present in the mush to accommodate strain during magmatic faulting, folding, and stoping of the xenolith blocks, but also a strong crystal framework to preserve the layering relatively intact, especially during deformation. In other words, the magma must be sufficiently rich in crystals and therefore denser than its surroundings to descend into the chamber, but equally be plastic enough to flow under strain, that is, behave as a visco-plastic material. (e.g., Bergantz et al., 2015; Schleicher et al., 2016).

In this context, a number of possible causes could trigger an extensive visco-plastic collapse of a magma mush: (1) differential cooling in the magma chamber, in which chamber margins cool faster than its interior, would promote the growth of crystal-rich solidification fronts that are prone to collapse into the hotter interior (Marsh, 1996, 2006, 2013, 2015; Žák and Paterson, 2010); (2) density inversion of crystal-rich peripheral mush over hotter crystal-poor interior magma could trigger magma avalanching preferentially in the upper part of the chamber (roof) or in irregular steep sections of the wall; (3) the arrival of a new magma batch could allow the crystal mush to unlock and fluidize (e.g., Solgadi and Sawyer, 2008; Burgisser and Bergantz, 2011; Paterson et al., 2016; Bergantz et al., 2017), which could contribute to magma avalanching either by magma injection to the solidification front that penetrates and spreads magma by porous media flow through the crystal mush, or by the fluid phase generating an excess pressure (by bubble formation) in the hydrogranular mixture (e.g., Sumita and Manga, 2008; Petford, 2009); (4) the presence of host-rock blocks and cognate inclusions in the margin could increase the overall density of the solidifying crystal-melt pile, whereby the erosive component of the magma avalanching process can act to remove earlier-formed parts of the margin (cognate inclusions) and increase the density of the magma pile, helping it to overcome the flow resistance of the medium (e.g., Paterson et al., 2016); and (5) natural seismic sources such as tectonic and volcanic earthquakes could induce destabilization by fluidization and decrease in pressure in the crystal mush (e.g., Sumita and Manga, 2008; Paterson et al., 2019, and references therein).

We envisage that most of the causes described for the development of large-scale (10^2–10^3-m-wide) magma avalanches in peripheral mush zones occur in large, long-lived magma-mush chambers that mechanically mingle and mix, rather than small, isolated magma bodies (e.g., Solgadi and Sawyer, 2008; Pinotti et al., 2016). A long-lived, thermally mature magmatic plumbing system allows potentially multiple magma chambers to form at shallow

crustal levels (e.g., Alasino et al., 2017). Thus, the generation of these multiple chambers by the ascent of different magma batches can be promoted by gravitational collapse and local convection of a ductile downward flow of the earlier magma mushes.

Implications for the Behavior of Long-Lived Magmatic Systems, and the Significance of Structural and Compositional Diversity in Upper-Crustal Magma Chambers

Uranium-lead (U-Pb) zircon geochronology illustrates that the SPIS is an example of a long-lived magmatic system, emplaced over at least 2.9 m.y., and possibly >8.1 m.y. (Leopold, 2016), comparable to other zoned intrusive suites across the Sierran crest (e.g., Coleman et al., 2004; Frazer et al., 2014; Paterson et al., 2016). Like other Sierran intrusive suites, the SPIS displays map-scale textural and compositional homogeneity within identified units (e.g., restricted Sr isotope values in the SPIS; Macias, 1996; Leopold, 2016). However, it displays remarkable mesoscale and microscale structural heterogeneity, the schlieren zone being a key example (see also Burgisser and Bergantz, 2011). Schlieren were created and deformed in the magmatic state. The scale of the schlieren zone, ~800 m wide, suggests that an extensive area of the crystal mush was mobilized at the outermost (oldest and coolest) margin of the SPIS. The complexity in the structure within a single outcrop suggests that multiple, repeated avalanche events took place with the avalanche area, or front, migrating inwards. Additionally, it suggests that this system was dynamic even at shallow crustal levels (2.0–3.5 ± 0.6 kbar; Macias, 1996).

The structurally complex schlieren zone suggests that a high level of instability and mobility existed at the margin zone of the granitic magma mush. Our field observations of magmatic faulting and magmatic fold structures are remarkably similar to the model observations from the magma "mixing bowl" of Bergantz et al. (2015). In addition, this model predicts that due to the hydrogranular behavior of the mush, variable gradients in porosity exist within the mush (Bergantz et al., 2015; Schleicher and Bergantz, 2017), which may explain the formation of the leucogranite dikes as well as the re-intrusion and reorganization of schlieren layers post-avalanching.

The schlieren zone at the KLG margin is one spectacular example of local compositional and structural diversity generated at the emplacement level, in an upper-crustal magma body. While the mineral components of schlieren and leucogranite layers are locally sourced from the host magma mush, dynamic processes operated to mechanically sort crystals by density and mode. The same dynamic processes (e.g., avalanching, mixing) may have also occurred in parts of the KLG unit where schlieren are sparse. KLG magma may have later erased these layers and/or modified them by protracted magma mixing, mobilization, and/or magma flow in hotter, more melt-rich areas of the chamber. This would reproduce the map-scale homogeneous appearance of the inner KLG, which experienced a slower cooling rate than the outermost margin. In the case of the schlieren zone at the KLG margin, however, a rich array of structures is preserved, perhaps capturing different magmatic conditions than found in other KLG domains.

CONCLUSIONS

Whole-rock data reveal that the granitic rocks of the Sonora Pass Intrusive Suite in the northern Sierra Nevada have a relatively narrow range of silica content (61%–71%) and show geochemical signatures typical of high-K calc-alkaline granites, with metaluminous to slightly peraluminous compositions.

Evidence presented here suggests that the southwestern intrusive margin of the KLG is a remarkable example of the dynamic processes that can occur along a pluton–wall rock contact. Large-scale downward magma avalanching events at an early-formed solidification front generated an ~800-m-wide region of igneous layering (schlieren and leucocratic bands) recording the complex interaction between magmatic structure formation and deformation at map to outcrop scales. Schlieren (SiO_2 = 54%–61%) were formed by the accumulation of medium-grained ferromagnesian minerals (hornblende + biotite), zircon, sphene, apatite, and opaque minerals, and minor plagioclase and interstitial quartz. Associated leucocratic bands (SiO_2 = 66%–69%) are dominated by coarse-grained feldspar (plagioclase over microcline) + quartz with minor ferromagnesian and accessory minerals and secondary muscovite, and potentially formed by a mix of melt removed from schlieren with melt remaining in the surrounding host. A third group of rocks defined as leucogranite (SiO_2 = 73%) are found in dikes that intrude schlieren packages. They have a similar mineralogy to the leucocratic bands but are generally more felsic in composition. The leucogranite dikes may reflect the fractionated melts removed from schlieren.

Whole-rock chemical data support that the main mechanism of formation of schlieren and leucocratic bands was by fractional crystallization in an isotopically closed system, mainly by an effective segregation of mafic minerals plus accessory phases with drainage and diffusion of leucogranitic melts back into the KLG. The accumulation of mafic and accessory minerals along steep walls displaced the intergranular felsic melt toward the interior of the pluton or to shallower levels of the plumbing system by deformation-assisted mechanical separation in the hydrogranular medium, promoted by both gravity and local convection. This process was repeated and episodic, which allowed mixing, magmatic erosion and recycling, re-intrusion, and magmatic deformation (faulting and folding) to occur at the KLG margin.

ACKNOWLEDGMENTS

Financial support was provided by the National Science Foundation grant EAR-1624847 to S.R. Paterson and a CONICET (Argentine National Council of Scientific and Technical Research) external fellowship awarded to P.H. Alasino for his research stay at the University of Southern California, Los Angeles, California, USA. L. Ardill and K. O'Rourke are thanked for the assistance in mapping work. We thank M. Holness (University of Cambridge) and an anonymous reviewer for their very constructive reviews that significantly improved the manuscript. We also would like to thank A. Whittington (editor) for his helpful comments and suggestions on our manuscript.

REFERENCES CITED

Alasino, P.H., Larrovere, M.A., Rocher, S., Dahlquist, J.A., Basei, M.A.S., Memeti, V., Paterson, S., Galindo, C., Grande, M.M., and da Costa Campos Neto, M., 2017, Incremental growth of an upper crustal, A-type pluton, Argentina: Evidence of a re-used magma pathway: Lithos, v. 284–285, p. 347–366, https://doi.org/10.1016/j.lithos.2017.04.013.

Armstrong, R.L., and Ward, P.L., 1993, Late Triassic to earliest Eocene magmatism in the North American Cordillera: Implications for the Western Interior Basin, *in* Caldwell, W.G.E., and Kauffman, E.G., eds., Evolution of the Western Interior Basin: Geological Association of Canada Special Paper 39, p. 49–72.

Bachmann, O., and Bergantz, G.W., 2008, Deciphering magma chamber dynamics from styles of compositional zoning in large silicic ash flow sheets: Reviews in Mineralogy and Geochemistry, v. 69, p. 651–674, https://doi.org/10.2138/rmg.2008.69.17.

Barbey, P., Gasquet, D., Pin, C., and Bourgeix, A.L., 2008, Igneous banding, schlieren and mafic enclaves in calc-alkaline granites: The Budduso pluton (Sardinia): Lithos, v. 104, p. 147–163, https://doi.org/10.1016/j.lithos.2007.12.004.

Bateman, P.C., 1992, Plutonism in the central part of Sierra Nevada batholith, California: U.S. Geological Survey Professional Paper 1483, 186 p., https://doi.org/10.3133/pp1483.

Bergantz, G.W., 2000, On the dynamics of magma mixing by reintrusion: Implications for pluton assembly processes: Journal of Structural Geology, v. 22, p. 1297–1309, https://doi.org/10.1016/S0191-8141(00)00053-5.

Bergantz, G.W., and Ni, J., 1999, A numerical study of sedimentation by dripping instabilities in viscous fluids: International Journal of Multiphase Flow 25, v. 2, p. 307–320, https://doi.org/10.1016/S0301-9322(98)00050-0.

Bergantz, G.W., Schleicher, J.M., and Burgisser, A., 2015, Open-system dynamics and mixing in magma mushes: Nature Geoscience, v. 8, p. 793–796, https://doi.org/10.1038/ngeo2534.

Bergantz, G.W., Schleicher, J.M., and Burgisser, A., 2017, On the kinematics and dynamics of crystal-rich systems: Journal of Geophysical Research: Solid Earth, v. 122, p. 6131–6159, https://doi.org/10.1002/2017JB014218.

Blanchette, F., Peacock, T., and Bush, J.W.M., 2004, The Boycott effect in magma chambers: Geophysical Research Letters, v. 31, L05611, https://doi.org/10.1029/2003GL019235.

Broxton, D.E., Warren, R.G., Byers, F.M., and Scott, R.B., 1989, Chemical and mineralogic trends within the Timber Mountain–Oasis Valley Caldera Complex, Nevada: Evidence for multiple cycles of chemical evolution in a long-lived silicic magma system: Journal of Geophysical Research, v. 94, p. 5961–5986, https://doi.org/10.1029/JB094iB05p05961.

Burgisser, A., and Bergantz, G.W., 2011, A rapid mechanism to remobilize and homogenize crystalline magma bodies: Nature, v. 471, p. 212–215, https://doi.org/10.1038/nature09799.

Cao, W., Paterson, S., Memeti, V., Mundil, R., Anderson, J.L., and Schmidt, K., 2015, Tracking paleodeformation fields in the Mesozoic central Sierra Nevada arc: Implications for intra-arc cyclic deformation and arc tempos: Lithosphere, v. 7, p. 296–320, https://doi.org/10.1130/L389.1.

Christensen, J.N., Halliday, A.N., Lee, D.-C., and Hall, C.M., 1995, In situ Sr isotopic analysis by laser ablation: Earth and Planetary Science Letters, v. 136, p. 79–85, https://doi.org/10.1016/0012-821X(95)00181-6.

Coleman, D.S., Gray, W., and Glazner, A.F., 2004, Rethinking the emplacement and evolution of zoned plutons: Geochronologic evidence for incremental assembly of the Tuolumne Intrusive Suite, California: Geology, v. 32, p. 433–436, https://doi.org/10.1130/G20220.1.

Cooper, K.M., and Reid, M.R., 2003, Re-examination of crystal ages in recent Mount St. Helens lavas: Implications for magma reservoir processes: Earth and Planetary Science Letters, v. 213, p. 149–167, https://doi.org/10.1016/S0012-821X(03)00262-0.

Costa, F., Chakraborty, S., and Dohmen, R., 2003, Diffusion coupling between trace and major elements and a model for calculation of magma residence times using plagioclase: Geochimica et Cosmochimica Acta, v. 67, p. 2189–2200, https://doi.org/10.1016/S0016-7037(02)01345-5.

Davidson, J., Tepley, F., III, Palacz, Z., and Meffan-Main, S., 2001, Magma recharge, contamination and residence times revealed by in situ laser ablation isotopic analysis of feldspar in volcanic rocks: Earth and Planetary Science Letters, v. 184, p. 427–442, https://doi.org/10.1016/S0012-821X(00)00333-2.

Davidson, J.P., Font, L., Charlier, B.L.A., and Tepley, F.J., 2008, Mineral-scale Sr isotope variation in plutonic rocks: A tool for unraveling the evolution of magma systems: Transactions of the Royal Society of Edinburgh: Earth Sciences, v. 97, p. 35–67, https://doi.org/10.1017/S0263593300001504.

Davis, M., Koenders, M.A., and Petford, N., 2007, Vibro-agitation of chambered magma: Journal of Volcanology and Geothermal Research, v. 167, p. 24–36, https://doi.org/10.1016/j.jvolgeores.2007.07.012.

DeCelles, P.G., Ducea, M.N., Kapp, P., and Zandt, G., 2009, Cyclicity in Cordilleran orogenic systems: Nature Geoscience, v. 2, p. 251–257, https://doi.org/10.1038/ngeo469.

de Silva, S., Zandt, G., Trumbull, R., Viramonte, J.G., Salas, G., and Jiménez, N., 2006, Large ignimbrite eruptions and volcano-tectonic depressions in the Central Andes: A thermomechanical perspective, *in* Troise, C., De Natale, G., and Kilburn, C.R.J., eds., Mechanisms of Activity and Unrest at Large Calderas: Geological Society of London Special Publication 269, p. 47–63, https://doi.org/10.1144/GSL.SP.2006.269.01.04.

Fourcade, S., and Allegre, C.J., 1981, Trace elements behavior in granite genesis—A case study: The calc-alkaline plutonic association from the Querigut complex (Pyrénées, France): Contributions to Mineralogy and Petrology, v. 76, p. 177–195, https://doi.org/10.1007/BF00371958.

Frazer, R.E., Coleman, D.S., and Mills, R.D., 2014, Zircon U-Pb geochronology of the Mount Givens Granodiorite: Implications for the genesis of large volumes of eruptible magma: Journal of Geophysical Research: Solid Earth, v. 119, p. 2907–2924, https://doi.org/10.1002/2013JB010716.

Giusso, J.R., 1981, Preliminary geologic map of the Sonora Pass 15-minute quadrangle, California: U.S. Geological Survey Open-File Report 81-1170, scale 1:62,500.

Hickey, R.L., Frey, F.A., Gerlach, D.C., and Lopez-Escobar, L., 1986, Multiple sources for basaltic arc rocks from the southern volcanic zone of the Andes (34°–41°S): Trace element and isotopic evidence for contributions from subducted oceanic crust, mantle, and continental crust: Journal of Geophysical Research: Solid Earth, v. 91, p. 5963–5983, https://doi.org/10.1029/JB091iB06p05963.

Hodson, M.E., 1998, The origin of igneous layering in the Nunarssuit syenite, South Greenland: Mineralogical Magazine, v. 62, p. 9–27, https://doi.org/10.1180/002646198547431.

Holness, M.B., Clemens, J.D., and Vernon, R.H., 2018, How deceptive are microstructures in granitic rocks? Answers from integrated physical theory, phase equilibrium, and direct observations: Contributions to Mineralogy and Petrology, v. 173, https://doi.org/10.1007/s00410-018-1488-8.

Huber, N.K., 1983, Preliminary geologic map of the Pinecrest quadrangle, central Sierra Nevada, California: U.S. Geological Survey Miscellaneous Field Studies Map MF-1437, scale 1:62,500.

Humphreys, M.C.S., and Holness, M.B., 2010, Melt-rich segregations in the Skaergaard Marginal Border Series: Tearing of a vertical silicate mush: Lithos, v. 119, p. 181–192, https://doi.org/10.1016/j.lithos.2010.06.006.

Irvine, T.N., 1987, Layering and related structures in the Duke Island and Skaergaard intrusions: Similarities, differences, and origins, *in* Parsons, I., ed., Origins of Igneous Layering: Dordrecht, D. Reidel Publishing Company, NATO ASI Series C196, p. 185–245, https://doi.org/10.1007/978-94-017-2509-5_6.

Irvine, T.N., Andersen, J.C.O., and Brooks, C.K., 1998, Included blocks (and blocks within blocks) in the Skaergaard intrusion: Geologic relations and the origins of rhythmic modally graded layers: Geological Society of America Bulletin, v. 110, p. 1398–1447, https://doi.org/10.1130/0016-7606(1998)110<1398:IBABWB>2.3.CO;2.

Jaupart, C., and Tait, S., 1995, Dynamics of differentiation in magma reservoirs: Journal of Geophysical Research, v. 100, p. 17,615–17,636, https://doi.org/10.1029/95JB01239.

John, D.A., 1983, Distribution, ages, and petrographic character of Mesozoic plutonic rocks, Walker Lake 1° by 2° quadrangle, California and Nevada: U.S. Geological Survey Miscellaneous Field Studies Map 1382-B, scale 1:250,000, https://doi.org/10.3133/mf1382B.

John, D.A., Schweickert, R.A., and Robinson, A.C., 1994, Granitic rocks in the Triassic-Jurassic magmatic arc of western Nevada and eastern California: U.S. Geological Survey Open-File Report 94-148, 61 p., https://doi.org/10.3133/ofr94148.

Kaiser, J.F., de Silva, S., Schmitt, A.K., Economos, R., and Sunagua, M., 2016, Million-year melt–presence in monotonous intermediate magma for a volcanic–plutonic assemblage in the Central Andes: Contrasting histories of crystal-rich and crystal-poor super-sized silicic magmas: Earth and Planetary Science Letters, v. 457, p. 73–86, https://doi.org/10.1016/j.epsl.2016.09.048.

Karakas, O., Degruyter, W., Bachmann, O., and Dufek, J., 2017, Lifetime and size of shallow magma bodies controlled by crustal-scale magmatism: Nature Geoscience, v. 10, p. 446–450, https://doi.org/10.1038/ngeo2959.

Kirsch, M., Paterson, S.R., Wobbe, F., Martínez Ardila, A.M., Clausen, B.L., and Alasino, P.H., 2016, Temporal histories of Cordilleran continental arcs: Testing models for magmatic episodicity: American Mineralogist, v. 101, p. 2133–2154, https://doi.org/10.2138/am-2016-5718.

Kistler, R.W., Chappell, B.W., Peck, D.L., and Bateman, P.C., 1986, Isotopic variation in the Tuolumne Intrusive Suite, central Sierra Nevada, California: Contributions to Mineralogy and Petrology, v. 94, p. 205–220, https://doi.org/10.1007/BF00592937.

Lackey, J.S., Cecil, M.R., Windham, C.J., Frazer, R.E., Bindeman, I.N., and Gehrels, G.E., 2012, The Fine Gold Intrusive Suite: The roles of basement terranes and magma source development

in the Early Cretaceous Sierra Nevada batholith: Geosphere, v. 8, p. 292–313, https://doi.org/10.1130/GES00745.1.
Lahren, M.M., and Schweickert, R.A., 1989, Proterozoic and Lower Cambrian miogeoclinal rocks of Snow Lake pendant, Yosemite-Emigrant Wilderness, Sierra Nevada, California: Evidence for major Early Cretaceous dextral translation: Geology, v. 17, p. 156–160, https://doi.org/10.1130/0091-7613(1989)017<0156:PALCMR>2.3.CO;2.
Lahren, M.M., Schweickert, R.A., Mattinson, J.M., and Walker, J.D., 1990, Evidence of uppermost Proterozoic to Lower Cambrian miogeoclinal rocks and the Mojave–Snow Lake fault: Snow Lake pendant, central Sierra Nevada, California: Tectonics, v. 9, p. 1585–1608, https://doi.org/10.1029/TC009i006p01585.
Le Maitre, R.W., ed., 1989, A Classification of Igneous Rocks and Glossary of Terms: Oxford, UK, Blackwell Scientific, 193 p.
Leopold, M.B., 2016, Structure, construction, and emplacement of the Late Cretaceous Sonora Pass intrusive suite: Central Sierra Nevada batholith, California [M.S. thesis]: San José, California, San José State University, 100 p.
Lowery Claiborne, L., Miller, C.F., Walker, B.A., Wooden, J.L., Mazdab, F.K., and Bea, F., 2006, Tracking magmatic processes through Zr/Hf ratios in rocks and Hf and Ti zoning in zircons: An example from the Spirit Mountain batholith, Nevada: Mineralogical Magazine, v. 70, p. 517–543, https://doi.org/10.1180/0026461067050348.
Macias, S.E., 1996, The Sonora Intrusive Suite: Constraints on the assembly of a Late Cretaceous, concentrically-zoned granitic pluton of the Sierra Nevada batholith [M.S. thesis]: Seattle, University of Washington, 66 p.
Marsh, B.D., 1996, Solidification fronts and magmatic evolution: Mineralogical Magazine, v. 60, p. 5–40, https://doi.org/10.1180/minmag.1996.060.398.03.
Marsh, B.D., 2006, Dynamics of magma chambers: Elements, v. 2, p. 287–292, https://doi.org/10.2113/gselements.2.5.287.
Marsh, B.D., 2013, On some fundamentals of igneous petrology: Contributions to Mineralogy and Petrology, v. 166, p. 665–690, https://doi.org/10.1007/s00410-013-0892-3.
Marsh, B.D., 2015, Magmatism, magma, and magma chambers, *in* Watts, A., ed., Treatise on Geophysics (second edition), Volume 6: Crustal and Lithosphere Dynamics: Oxford, Elsevier, p. 273–323, https://doi.org/10.1016/B978-0-444-53802-4.00116-0.
Martin, D., Griffiths, R.W., and Campbell, I.H., 1987, Compositional and thermal convection in magma chambers: Contributions to Mineralogy and Petrology, v. 96, p. 465–475, https://doi.org/10.1007/BF01166691.
Memeti, V., Paterson, S., Matzel, J., Mundil, R., and Okaya, D., 2010, Magmatic lobes as "snapshots" of magma chamber growth and evolution in large, composite batholiths: An example from the Tuolumne intrusion, Sierra Nevada, California: Bulletin of the Geological Society of America, v. 122, p. 1912–1931, https://doi.org/10.1130/B30004.1.
Middlemost, E.A., 1994, Naming materials in the magma/igneous rock system: Earth-Science Reviews, v. 37, p. 215–224, https://doi.org/10.1016/0012-8252(94)90029-9.
Paterson, S.R., 2009, Magmatic tubes, pipes, troughs, diapirs, and plumes: Late-stage convective instabilities resulting in compositional diversity and permeable networks in crystal-rich magmas of the Tuolumne batholith, Sierra Nevada, California: Geosphere, v. 5, p. 496–527, https://doi.org/10.1130/GES00214.1.
Paterson, S.R., and Ducea, M.N., 2015, Arc magmatic tempos: Gathering the evidence: Elements, v. 11, p. 91–98, https://doi.org/10.2113/gselements.11.2.91.
Paterson, S.R., Vernon, R.H., and Žák, J., 2005, Mechanical instabilities and physical accumulation of K-feldspar megacrysts in granitic magma, Tuolumne batholith, California, USA: Journal of the Virtual Explorer, Electronic Edition, v. 18, 1, https://doi.org/10.3809/jvirtex.2005.00114.
Paterson, S.R., Okaya, D., Memeti, V., Economos, R., and Miller, R.B., 2011, Magma addition and flux calculations of incrementally constructed magma chambers in continental margin arcs: Combined field, geochronologic, and thermal modeling studies: Geosphere, v. 7, p. 1439–1468, https://doi.org/10.1130/GES00696.1.
Paterson, S., Memeti, V., Mundil, R., and Žák, J., 2016, Repeated, multiscale, magmatic erosion and recycling in an upper-crustal pluton: Implications for magma chamber dynamics and magma volume estimates: American Mineralogist, v. 101, p. 2176–2198, https://doi.org/10.2138/am-2016-5576.
Paterson, S.R., Ardill, K., Vernon, R., and Žák, J., 2019, A review of mesoscopic magmatic structures and their potential for evaluating the hypersolidus evolution of intrusive complexes: Journal of Structural Geology, v. 125, p. 134–147, https://doi.org/10.1016/j.jsg.2018.04.022.
Petford, N., 2009, Which effective viscosity?: Mineralogical Magazine, v. 73, p. 167–191, https://doi.org/10.1180/minmag.2009.073.2.167.
Pinotti, L.P., D'Eramo, F.J., Weinberg, R.F., Demartis, M., Tubía, J.M., Coniglio, J.E., Radice, S., Maffini, M.N., and Aragón, E., 2016, Contrasting magmatic structures between small plutons and batholiths emplaced at shallow crustal level (Sierras de Córdoba, Argentina): Journal of Structural Geology, v. 92, p. 46–58, https://doi.org/10.1016/j.jsg.2016.09.009.
Ramos, F.C., and Reid, M.R., 2005, Distinguishing melting of heterogeneous mantle sources from crustal contamination: Insights from Sr isotopes at the phenocryst scale, Pisgah Crater, California: Journal of Petrology, v. 46, p. 999–1012, https://doi.org/10.1093/petrology/egi008.
Reid, J.B., Murray, D.P., Hermes, O.D., and Steig, E.J., 1993, Fractional crystallization in granites of the Sierra Nevada: How important is it?: Geology, v. 21, p. 587–590, https://doi.org/10.1130/0091-7613(1993)021<0587:FCIGOT>2.3.CO;2.
Rittmann, A., 1957, On the serial character of igneous rocks: Egyptian Journal of Geology, v. 1, p. 23–48.
Rocher, S., Alasino, P.H., Macchioli Grande, M., Larrovere, M.A., and Paterson, S.R., 2018, K-feldspar megacryst accumulations formed by mechanical instabilities in chamber margins, Asha pluton, NW Argentina: Journal of Structural Geology, v. 112, p. 154–173, https://doi.org/10.1016/j.jsg.2018.04.017.
Ruprecht, P., Bergantz, G.W., and Dufek, J., 2008, Modeling of gas-driven magmatic overturn: Tracking of phenocryst dispersal and gathering during magma mixing: Geochemistry Geophysics Geosystems, v. 9, Q07017, https://doi.org/10.1029/2008GC002022.
Schleicher, J.M., and Bergantz, G.W., 2017, The mechanics and temporal evolution of an open-system magmatic intrusion into a crystal-rich magma: Journal of Petrology, v. 58, p. 1059–1072, https://doi.org/10.1093/petrology/egx045.
Schleicher, J.M., Bergantz, G.W., Breidenthal, R.E., and Burgisser, A., 2016, Time scales of crystal mixing in magma mushes: Geophysical Research Letters, v. 43, p. 1543–1550, https://doi.org/10.1002/2015GL067372.
Slemmons, D.B., 1953, Geology of the Sonora Pass region [Ph.D. thesis]: Berkeley, University of California, 201 p.
Solgadi, F., and Sawyer, E.W., 2008, Formation of igneous layering in granodiorite by gravity flow: A field, microstructure and geochemical study of the Tuolumne Intrusive Suite at Sawmill Canyon, California: Journal of Petrology, v. 49, p. 2009–2042, https://doi.org/10.1093/petrology/egn056.
Steiger, R.H., and Jäger, E., 1977, Subcommission on Geochronology: Convention on the use of decay constants in geo- and cosmochronology: Earth and Planetary Science Letters, v. 1, p. 369–371, https://doi.org/10.1016/0012-821X(77)90060-7.
Stern, T.W., Bateman, P.C., Morgan, B.A., Newell, M.F., and Peck, D.L., 1981, Isotopic U-Pb ages of zircon from the granitoids of the central Sierra Nevada, California: U.S. Geological Survey Professional Paper 1185, 17 p., https://doi.org/10.3133/pp1185.
Sumita, I., and Manga, M., 2008, Suspension rheology under oscillatory shear and its geophysical implications: Earth and Planetary Science Letters, v. 269, p. 468–477, https://doi.org/10.1016/j.epsl.2008.02.043.
Sun, S.-s., and McDonough, W.F., 1989, Chemical and isotopic systematics of oceanic basalts: Implications for mantle composition and processes, *in* Saunders, A.D., and Norry, M.J., eds., Magmatism in the Ocean Basins: Geological Society of London Special Paper 42, p. 313–345, https://doi.org/10.1144/GSL.SP.1989.042.01.19.
Tanaka, T., Togashi, S., Kamioka, H., Amakawa, H., Kagami, H., Hamamoto, T., Yuhara, M., Orihashi, Y., Yoneda, S., Shimizu, H., Kunimaru, T., Takahashi, K., Yanagi, T., Nakano, T., Fujimaki, H., Shinjo, R., Asahara, Y., Tanimizu, M., and Dragusanu, C., 2000, JNdi-1: A neodymium isotopic reference in consistency with La Jolla neodymium: Chemical Geology, v. 168, p. 279–281, https://doi.org/10.1016/S0009-2541(00)00198-4.
Vernon, R.H., and Paterson, S.R., 2008, Mesoscopic structures resulting from crystal accumulation and melt movement in granites: Transactions of the Royal Society of Edinburgh: Earth Sciences, v. 97, p. 369–381, https://doi.org/10.1017/S0263593300001516.
Wahrhaftig, C., 1979, Significance of asymmetric schlieren for crystallization of granites in the Sierra Nevada batholith, California: Geological Society of America Abstracts with Programs, v. 11, p. 133.
Wahrhaftig, C., 2000, Geological map of the Tower Peak quadrangle, central Sierra Nevada, California: U.S. Geological Survey Miscellaneous Investigation Series Map I-2697, scale 1:62,500.
Wallace, G.S., and Bergantz, G.W., 2005, Reconciling heterogeneity in crystal zoning data: An application of shared characteristic diagrams at Chaos Crags, Lassen Volcanic Center, California: Contributions to Mineralogy and Petrology, v. 149, p. 98–112, https://doi.org/10.1007/s00410-004-0639-2.

Weinberg, R.F., Sial, R.N., and Pessoa, R.R., 2001, Magma flow within the Tavares pluton, northwestern Brazil: Compositional and thermal convection: Geological Society of America Bulletin, v. 113, p. 508–520, https://doi.org/10.1130/0016-7606(2001)113<0508:MFWTTP>2.0.CO;2.

Žák, J., and Klomínský, J., 2007, Magmatic structures in the Krkonoše–Jizera Plutonic Complex, Bohemian Massif: Evidence for localized multiphase flow and small-scale thermal-mechanical instabilities in a granitic magma chamber: Journal of Volcanology and Geothermal Research, v. 164, p. 254–267, https://doi.org/10.1016/j.jvolgeores.2007.05.006.

Žák, J., and Paterson, S.R., 2005, Characteristics of internal contacts in the Tuolumne Batholith, central Sierra Nevada, California (USA): Implications for episodic emplacement and physical processes in a continental arc magma chamber: Geological Society of America Bulletin, v. 117, p. 1242–1255, https://doi.org/10.1130/B25558.1.

Žák, J., and Paterson, S.R., 2010, Magmatic erosion of the solidification front during reintrusion: The eastern margin of the Tuolumne batholith, Sierra Nevada, California: International Journal of Earth Sciences, v. 99, p. 801–812, https://doi.org/10.1007/s00531-009-0423-7.